

CDH1 loss promotes diffuse-type gastric cancer tumorigenesis via epigenetic reprogramming and immune evasion

Gengyi Zou,^{1,†} Yuanjian Huang,^{1,2,†} Shengzhe Zhang,¹ Kyung-Pil Ko,¹ Bongjun Kim,¹ Jie Zhang,¹ Vishwa Venkatesan,¹ Melissa P. Pizzi,³ Yibo Fan,³ Sohee Jun,¹ Na Niu,⁶ Huamin Wang,⁷ Shumei Song,³ Jaffer A. Ajani,³ Jae-II Park^{1,4,5}

¹Department of Experimental Radiation Oncology, Division of Radiation Oncology, The University of Texas MD Anderson Cancer Center, Houston, TX 77030, USA

²Department of General Surgery, The First Affiliated Hospital of Nanjing Medical University, Nanjing, Jiangsu 210029, China

³Department of GI Medical Oncology, The University of Texas MD Anderson Cancer Center, Houston, TX 77030, USA

⁴Graduate School of Biomedical Sciences, The University of Texas MD Anderson Cancer Center, Houston, TX 77030, USA

⁵Program in Genetics and Epigenetics, The University of Texas MD Anderson Cancer Center, Houston, TX 77030, USA

⁶Department of Pathology, Yale School of Medicine, New Haven, CT 06510, USA

⁷Department of Pathology, Division of Pathology/Lab Medicine, The University of Texas MD Anderson Cancer Center, Houston, TX 77030, USA

[†]These authors contributed equally.

[‡]Correspondence: Jae-II Park (jaeil@mdanderson.org)

Tel: 713-792-3659; Fax: 713-794-5369

Keywords: CDH1, E-Cadherin, gastric cancer, gastric organoids, diffuse-type gastric adenocarcinoma, immune landscape remodeling, immune evasion, single-cell transcriptomics, cancer subtyping, EZH2

27 **Summary**

28
29 This study investigates diffuse-type gastric adenocarcinoma (DGAC), a deadly and
30 treatment-resistant cancer. It reveals that CDH1 inactivation occurs in a subset of
31 DGAC patient tumors, leading to the identification of two distinct DGAC subtypes. The
32 findings emphasize the importance of understanding DGAC's molecular diversity for
33 personalized medicine in patients with CDH1 inactivation.

34

35 **Abstract**

36 Diffuse-type gastric adenocarcinoma (DGAC) is a deadly cancer often diagnosed late
37 and resistant to treatment. While hereditary DGAC is linked to *CDH1* gene mutations,
38 causing E-Cadherin loss, its role in sporadic DGAC is unclear. We discovered *CDH1*
39 inactivation in a subset of DGAC patient tumors. Analyzing single-cell transcriptomes in
40 malignant ascites, we identified two DGAC subtypes: DGAC1 (*CDH1* loss) and DGAC2
41 (lacking immune response). DGAC1 displayed distinct molecular signatures, activated
42 DGAC-related pathways, and an abundance of exhausted T cells in ascites. Genetically
43 engineered murine gastric organoids showed that *Cdh1* knock-out (KO), *Kras*^{G12D},
44 *Trp53* KO (EKP) accelerates tumorigenesis with immune evasion compared to *Kras*^{G12D},
45 *Trp53* KO (KP). We also identified EZH2 as a key mediator promoting *CDH1* loss-
46 associated DGAC tumorigenesis. These findings highlight DGAC's molecular diversity
47 and potential for personalized treatment in *CDH1*-inactivated patients.

48

49 **Introduction**

50 Gastric adenocarcinoma (GAC) is the 4th most common cause of cancer deaths
51 worldwide (Sung et al., 2021). GAC is mainly divided into intestinal-type gastric
52 adenocarcinoma (IGAC, 50%), diffuse-type gastric adenocarcinoma (DGAC, 30%), and
53 mixed (Iyer et al., 2020). DGAC is histologically characterized by poor differentiation,
54 loss of cell adhesion proteins, fibrosis, and infiltration. Unlike IGAC, DGAC is relatively
55 more often observed in younger, female, and Hispanic population than in older, male,
56 and non-Hispanic ones (Chen et al., 2016; Wang et al., 2020). While the incidence of
57 IGAC has declined due to H. Pylori (HP) therapy and lifestyle improvements over the
58 past few decades, the number of DGAC cases has remained constant or has risen
59 (Henson et al., 2004; Assumpcao et al., 2020).

60 DGAC tends to metastasize to the peritoneal cavity, which makes it difficult to
61 diagnose early by imaging. In addition, isolated tumor cells or small clusters of tumor
62 cells infiltrate in unpredictable patterns. Thus, DGAC is often detected at a late stage,
63 leading to a poor prognosis. For such patients, curative resection is not possible.
64 Systemic therapy is the main option for potentially prolonging survival and improving
65 symptoms (Muro et al., 2019; Ajani et al., 2022). Despite the distinct features of DGAC
66 in both a molecular basis and therapy resistance, the first-line treatment options are not
67 specific for DGAC (Garcia-Pelaez et al., 2021; Ajani et al., 2022). Systemic therapy with
68 targeted therapy has shown limited benefits (Selim et al., 2019; Korfer et al., 2021). In
69 parallel, immune checkpoint inhibitors (ICIs) have been used recently. The advent of
70 first-generation ICIs that target Cytotoxic T-Lymphocyte Antigen 4 (CTLA4) and
71 Programmed death-ligand (PD-L1) has brought a paradigm shift in the treatment of
72 various advanced cancers (Mazzarella et al., 2019). Nivolumab (PD-1 inhibitor) can be
73 either combined with chemotherapy as first-line treatment or used as monotherapy as
74 later-line treatment in Asia (Boku et al., 2021; Janjigian et al., 2021). Pembrolizumab
75 (PD-1 inhibitor) showed a promising outcome treating GAC with high microsatellite
76 instability or high tumor mutational burden (Wainberg et al., 2021). However, DGAC
77 imposes major difficulty in the clinic and available therapies perform poorly. Generally,
78 DGAC has immunosuppressed stroma and is genetically stable (Teng et al., 2015; Ge
79 et al., 2018). Given the limited therapeutic options for DGAC, it is imperative to
80 understand the biology of DGAC, which may establish a groundwork for developing new
81 targeted therapies for DGAC. Furthermore, for maximizing therapeutic efficacy, it is
82 crucial to identify patients who can most benefit from specific treatment options.
83 Nevertheless, to date, DGAC patient stratification by molecular signatures has not been
84 achieved.

85 Hereditary DGAC, as a minor proportion of DGAC (1–3%), is mainly
86 characterized by germline mutations in the *CDH1* gene that encodes E-Cadherin (Blair
87 et al., 2020). However, other than hereditary DGAC, the role of *CDH1* loss in DGAC
88 tumorigenesis is unclear. Cell-to-cell adhesion is a crucial phenomenon for maintaining
89 tissue morphogenesis and homeostasis, as well as for regulating cell differentiation,

90 survival, and migration. E-Cadherin mediates cell-to-cell adhesion, which is essential for
91 determining the proliferation specificity and differentiation of epithelial cells and
92 preventing invasion (van Roy and Berx, 2008). To understand the impact of *CDH1* loss
93 on DGAC tumorigenesis, we analyzed single-cell transcriptomes of cryopreserved
94 peritoneal carcinomatosis (PC) from 19 DGAC patients and identified two subtypes of
95 DGACs exhibiting specific molecular signatures including E-Cadherin loss and immune
96 landscape remodeling. To further verify our in-silico analysis, we generated and
97 characterized a genetically engineered gastric organoid (GO) model that recapitulates
98 E-Cadherin inactivation-associated DGAC tumorigenesis. This study stratifies DGAC
99 patients by single-cell transcriptomics and elucidates the unexpected role of E-Cadherin
100 loss in transcriptional reprogramming and immune evasion, providing novel insights into
101 E-Cadherin loss-associated DGAC tumorigenesis.

102

103

Results

104

CDH1 inactivation in DGAC

105
106
107
108
109
110
111
112
113
114
115
116
117
118
119
120
121
122
123
124
125
126
127
128
129
130
131
132
133
134
135
136
137
138
139
140
141
142
143
144

To explore the role of CDH1 in DGAC tumorigenesis, we examined the genetic alterations and protein levels of CDH1 in DGAC. According to cBioPortal, 25% of tumor from the DGAC patients showed *CDH1* gene alterations, including mutations and deep deletions (**Fig. 1A**). We also assessed the CDH1 protein expression in the tissue microarray of 114 DGAC patients' tumor samples (patient information was listed in **Table S4**). Immunohistochemistry (IHC) showed that 37.72% of DGAC patients were CDH1 negative, 37.72% exhibited low CDH1 expression, and 24.56% displayed high CDH1 expression (**Fig. 1B**), which was also quantified with histochemical scoring assessment (H-score) of each slide (**Fig. 1C**). Next, we determined the transcriptional signature of DGAC at the single-cell transcriptomics level by analyzing single-cell RNA-seq (scRNA-seq) datasets of PC cells from 19 stage IV DGAC patients (**Fig. 1D, Table S5**) (Wang et al., 2021). After data integration and normalization, a total of 30 cell clusters were generated according to distinctive gene expression patterns (**Fig. 1E, fig. S1A, B, Table S6**). We re-clustered the datasets as the mega clusters according to Leiden-based UMAP (**Fig. 1F**). To conduct the precise subtyping of DGAC, we reanalyzed the scRNA-seq datasets with only epithelial cells (**Fig. 1G, fig. S1C, Table S7**). An unsupervised pair-wise correlation analysis showed that the combined datasets of 19 DGAC patients were divided into two major subtypes (DGAC1 and DGAC2) (**Fig. 1H**). To comparatively analyze DGAC 1 and 2 according to their clinical information (**Table S5**), we have thoroughly examined the available data and compared various clinical and pathological features between the two subtypes. Upon analysis, we did not observe significant differences in survival time, race, gender, or age between DGAC1 and DGAC2 subtypes (**fig. S1D, S1E, S1G, and S1I**). Regarding pathological features, DGAC1 had a higher proportion (DGAC1: 3/11, 27.3%; DGAC2: 1/8, 12.5%) of patients with non-signet ring cell carcinoma (**fig. S1F**). A notable distinction in metastatic sites was displayed. DGAC1 patients exhibited a higher prevalence of metastatic sites compared to DGAC2. This observation suggests potential differences in the metastatic behavior of the two subtypes (**fig. S1H**). The transcriptional signature of DGAC1 epithelial cell clusters was distinct from that of DGAC2 (**Fig. 1I, J, and Table S8**). In line with the heterogeneity of CDH1's genomic alterations and expression in DGAC patients (**Fig. 1A, B**), the DGAC1 subtype exhibited a relatively lower expression of *CDH1* compared to DGAC2 (**Fig. 1K, L**), indicating that the unsupervised pair-wise subtyping can also stratify DGAC patients by *CDH1* expression. While tissue microarray analysis showed that within the cohort of 114 DGAC patients, where 37.7% of patients exhibit low CDH1 levels (**Fig. 1B, C**), this subset of patients may have been classified into DGAC1 or DGAC2 based on the differential expression of other signature genes specific to each cluster, rather than solely relying on CDH1 expression. We also identified the molecular signatures of DGAC1 and DGAC2 (**Fig. 1M**). The gene list for calculating signature scores, including the DGAC1 and DGAC2 signatures, comprised the top 50 highly variable genes from each subgroup. (**Fig. 1M, Table S8**). These

145 results identify two distinct subtypes of DGACs by distinct molecular signatures and
146 CDH1 expression.

147

148 Molecular characterization of DGAC subtypes

149 Next, we characterized the molecular subtypes of DGAC. Given that E-Cadherin
150 downregulation is commonly observed in epithelial tumors and is a hallmark of the
151 epithelial to mesenchymal transition (EMT), we checked the EMT scores based on the
152 established gene set (**Table S9**). DGAC1 showed a higher EMT score compared to
153 DGAC2 (**fig. S1J**). Extensive genomic analyses of GAC have found that DGACs display
154 distinct activation of signaling pathways different from IGACs (Ooki and Yamaguchi,
155 2022). By scRNA-seq-based signaling scoring, we observed that the FGFR2, HIPPO,
156 PI3K/AKT/MTOR, and TGFBETA pathways were enriched in DGAC1, which
157 corresponds to decreased CDH1 expression compared to DGAC2 (**fig. S1K, S1P, S1M,**
158 **and S1R**). Additionally, we noted that FGFR1 is inversely correlated with CDH1
159 expression and enriched in DGAC1 (**fig. S1L**). Conversely, the RHOA and MAPK
160 pathways were enriched in DGAC2 (**fig. S1N, S1O, and S1Q**). Additionally, we
161 analyzed the copy number variation (CNV) of DGACs by using normal stomach
162 samples as a reference. We combined 29 scRNA-seq datasets of normal stomach
163 samples (Normal) with the previous 19 DGAC patients (Kim et al., 2022) (**fig. S2A**).
164 Except for the endothelial cell markers, the same marker panel was utilized as the
165 previous DGAC subcategory process to annotate the cells into epithelial cells, myeloid
166 cells, B cells, plasma cells, T cells, effector T cells, naïve T cells, exhausted T cells,
167 fibroblasts, and endothelial cells (**fig. S1A, S2B, and S2C**). Leiden-based UMAP
168 exhibited the same cell types as the DGAC stratification analysis (**fig. S2D, S2E, and**
169 **Table S10**), except that the endothelial cell cluster appeared due to the normal tissue
170 (**fig. S2C**). According to the previously identified DGAC subgroups, we separated the
171 UMAP as Normal, DGAC1, and DGAC2 (**fig. S2F, fig. S2G**). Although the epithelial
172 cells were defined as EPCAM^{high} clusters among all groups, epithelial cells from the
173 Normal group were clearly isolated from the major epithelial cell population of the
174 merged datasets (**fig. S2G**). CNV patterns were different between DGAC1 and DGAC2
175 (**fig. S2H**). We observed notable differences between DGAC1 and DGAC2 regarding
176 copy number gains (GOF) on specific chromosomes. In DGAC1, we observed more
177 pronounced copy number gains on chromosomes 3, 9, 19, and X, while in DGAC2,
178 there were increased copy number gains on chromosomes 1, 8, 11, 17, 20, and 21.
179 These differences in copy number alterations were found to be statistically significant,
180 as indicated by the adjusted *P* values (**fig. S2I, S2J**). These results indicate the
181 heterogeneity of DGAC with differentially activated signaling pathways.

182

183 **Immune landscape remodeling with T cell exhaustion in DGAC1**

184 Having determined the molecular signatures of DGAC tumor cells, we next analyzed
185 immunological response associated with DGAC ascites. Intriguingly, scRNA-seq-based
186 immune cell profiling showed that compared to DGAC2 where immune cells barely
187 existed, DGAC1 was highly enriched with immune cells, including T cells, B cells, and
188 myeloid cells (**Fig. 2A-C, fig. S2K-L**). Additionally, we examined cellular networks
189 among all cell clusters (DGAC1 vs. DGAC2) using a CellChat package that infers cell-
190 to-cell functional interaction based on ligand-receptor expression (Jin et al., 2021).
191 Compared to DGAC2, DGAC1 showed relatively more inferred interactions among
192 different cell types (**Fig. 2D**). According to the differential number of interactions, the
193 interactions between fibroblast and epithelial and endothelial cells were decreased,
194 while widespread increased interactions were found in DGAC1 compared to DGAC2
195 (**Fig. 2E**). Notably, exhausted T cells, as a receiver, showed the most increased
196 interactions compared with other T cells in DGAC1, which is the major population
197 among all immune cells (**Fig. 2F**). Gene Set Enrichment Analysis (GSEA) identified the
198 pathways that are enriched in DGAC1 with six gene sets, including Gene sets derived
199 from the Gene Ontology Biological Process (GOBP), and five canonical pathways gene
200 sets (REACTOME, WP, BIOCARTA, PID, and KEGG) (**fig. S3A-F, Table S11-S16**).
201 Except for REACTOME (**fig. S3B**), T cell-related immune response pathways were
202 enriched in DGAC1 based on the other five gene sets (**fig. S3A, S3C, S3D-F**).
203 Consistent with the CellChat prediction and GSEA results, DGAC1 showed the
204 significant upregulation of T cell exhaustion markers (LAG3, TIGIT, CTLA4, and
205 HAVCR2) and the increased T cell exhaustion score, compared to DGAC2 (**Fig. 2G-I**).
206 Similarly, immune checkpoints-related genes (CTLA4, PDCD1, PDCD1LG2, and
207 CD274) and their score were markedly upregulated in DGAC1 over DGAC2 (**Fig. 2J-L**).
208 In addition to T cell analysis, we also examined myeloid-derived suppressor cells
209 (MDSC) and macrophage polarization. MDSC score is relatively higher in DGAC1 than
210 DGAC2 (**Fig. 2M-O**). Meanwhile, most of M1 and M2 macrophage polarization maker
211 expression is enriched in DGAC1 compared to DGAC2 (**fig. S3G-H**). These results
212 suggest that compared to DGAC2, the DGAC1 subtype exhibits distinct immune
213 remodeling featured by T cell exhaustion and increased expression of the genes
214 associated with immune checkpoints.

215

216 **Cdh1 loss induces neoplasia in conjunction with *Trp53* KO and *Kras*^{G12D}**

217 To validate the in silico results, we utilized murine GOs that enable multiple genetic
218 engineering with immediate phenotype analyses. *Cdh1* deficiency results in early-stage
219 DGAC phenotype in a mouse model (Mimata et al., 2011; Hayakawa et al., 2015).
220 Nevertheless, other genes need to be included to recapitulate DGAC tumorigenesis.
221 The genes encoding the receptor tyrosine kinase (RTK)-RAS signaling pathway and the

222 *TP53* gene were profoundly disrupted in DGAC (Cancer Genome Atlas Research, 2014;
223 Cristescu et al., 2015). *KRAS* and *TP53* were genetically altered in 13.19% and 36.11%
224 of DGAC cases, respectively, as per cBioPortal analysis (**Fig. 3A**). Furthermore, we
225 observed that the PI3K/AKT/mTOR pathway is activated in DGAC1 (**fig. S1M**).
226 Therefore, to create preneoplastic or neoplastic conditions to determine the impact of
227 CDH1 loss on DGAC tumorigenesis (Till et al., 2017), we genetically manipulated three
228 genes (*Cdh1*, *Trp53*, and *Kras*) in GOs. Briefly, from the *Cdh1* wild type (WT) and *Kras*
229 *LSL-G12D/+*; *Trp53*^{f/f} mice, gastric epithelial cells were isolated to culture them into GOs
230 (**Fig. 3B**). Subsequently, using the Cre-LoxP recombination and CRISPR-based genetic
231 manipulation, we established two lines of GOs carrying *Kras*^{G12D/+} and *Trp53* deletion in
232 combination with *Cdh1* KO (KP: *Kras*^{G12D/+}; *Trp53* KO [KP], *Cdh1*/*E-Cadherin* KO;
233 *Kras*^{G12D/+}; *Trp53* KO [EKP]) (**Fig. 3B**). Genetic modifications were validated by PCR-
234 based genotyping and genomic DNA sequencing and immunofluorescence (IF) staining
235 (**fig. S4A-C**, **Fig. 3G**). Meanwhile, we monitored their sizes and numbers by
236 macroscopic analyses during passages to maintain the stable culture process during
237 passages (**Fig. 3C, D**). Unlike WT GOs growing as a single layer of epithelial cells, KP
238 and EKP GOs displayed multilayered epithelium (**Fig. 3E**). Notably, compared to WT
239 and KP, EKP GOs exhibited abnormal morphology such as vacuolization and cell
240 adhesion loss along with cell hyperplasia (**Fig. 3E**). Additionally, EKP GOs were
241 hyperproliferative compared to WT and KP GOs, assessed by immunostaining of
242 MKI67, a cell proliferation marker (**Fig. 3F, H**).

243 We next interrogated the mechanism of *Cdh1* loss-associated DGAC
244 tumorigenesis by performing multiplex scRNA-seq of WT, KP, and EKP GOs (**fig. S4D**).
245 Each group was tagged with two Cell Multiplexing Oligo (CMO) tags, then pooled
246 together with the same number of cells after being counted. All datasets were integrated
247 with the Harmony algorithm (Korsunsky et al., 2019) to minimize the batch effect (**fig.**
248 **S4E**). WT, KP, and EKP GOs were merged well in a batch-based UMAP (**Fig. 3I**). To
249 identify the gene signature of each cell cluster, we generated a heatmap to calculate the
250 top 5,000 highly variable genes (**fig. S4F**). Each UMAP and heatmap represented the
251 different cell distribution among three types of GOs (**Fig. 3J, K, fig. S4G-I, and Table**
252 **S17**). Notably, Aquaporin 5 (Aqp5), a gastric tissue stem cell marker (Tan et al., 2020),
253 was decreased in EKP compared to WT and KP (**Fig. 3K**).

254 To determine the pathological relevance of EKP GOs with human DGAC, we
255 utilized a single-cell inferred site-specific omics resource (Scissor) analysis (Sun et al.,
256 2022) and assessed the transcriptomic similarity between of EKP GOs and the bulk
257 RNA-seq data of patients diagnosed with DGAC from the TCGA database. While using
258 WT organoids as a reference and comparing the transcriptional signature, we observed
259 that EKP organoids displayed similarities in gene expression features of human DGAC
260 (**Fig. 3L**). To determine the subtype similarity, we compared the EKP scRNA-seq data
261 with our own datasets (DGAC1 and DGAC2) rather than relying solely on the TCGA
262 database. The analysis revealed that EKP organoids exhibited a greater resemblance to
263 DGAC1 transcriptional signature compared to DGAC2 (**Fig. 3M**). Next, by comparing

264 the expression levels of DGAC1 and DGAC2 signatures in EKP (**Fig. 1M**), we observed
265 a higher presence of DGAC1 signature compared to DGAC2 (**Fig. 3N**). These data
266 suggest that CDH1 loss combined with TP53 inactivation and KRAS hyperactivation
267 (EKP) is sufficient to induce transformation and EKP organoids display similar
268 transcriptional features to DGAC1, indicating pathological relevance of EKP GOs to
269 human DGAC.

270

271 ***Cdh1* KO induces immune evasion of tumor cells**

272 Having determined distinct immune remodeling with T cell exhaustion in the DGAC1
273 subtype where CDH1 is downregulated (**Fig. 2**), we asked whether genetic ablation of
274 *CDH1* contributes to immune evasion of DGAC. To test this, we established KP and
275 EKP GO-derived cell lines in 2D culture with minimum growth factors (culture medium:
276 DMEM Complete Medium with 10% fetal bovine serum) for allograft transplantation
277 (**Fig. 4A**). Unlike WT GOs that failed to grow in 2D culture, both KP and EKP cells grew
278 in 2D culture and were maintained well at multiple passages. Then, KP and EKP cell
279 lines derived from C57BL/6 strain were used for transplantation into C57BL/6 mice. The
280 morphological characteristics of KP and EKP cells exhibited notable differences. KP
281 cells exhibited a compact and tightly packed phenotype, forming densely clustered
282 colonies, while EKP cells displayed a more loosely-arranged and dispersed
283 morphology, lacking the cohesive structure of KP cells (**Fig. 4A**). Of note, there was no
284 significant difference in cell proliferation between KP and EKP cells (**Fig. 4B**). However,
285 transplantation results showed that tumor incidence and volume of EKP tumors was
286 markedly higher than KP tumors (tumor incidence rates: EKP [91.7%] vs. KP [16.7%])
287 (**Fig. 4C-E**). Histologically, EKP tumors exhibited poorly differentiated tumor cells, the
288 feature of DGAC (**Fig. 4F**) with CDH1 loss (**Fig. 4H**) and increased cell proliferation
289 (**Fig. 4G, I**).

290 To further determine the impact of CDH1 loss on immune evasion, we performed
291 the immunostaining of KP and EKP tumors. We observed CD3 (a marker for all T cells),
292 CD4 (a marker for helper T cells), and TIM3 (a marker for exhausted T cells) are
293 enriched in EKP tumor cortex compared with KP cortex (**Fig. 4J, 4K, 4N, 4P, 4Q, and**
294 **4T**), and the CD8 (a marker for killer T cells) expression is similar between KP and EKP
295 tumors (**Fig. 4L and 4R**). PDCD1, a marker for exhausted T cells, showed increased
296 expression in the middle and cortex of EKP compared with the same part of KP tumors
297 (**Fig. 4M and 4S**). Furthermore, we performed LY6G (a marker for MDSCs) and CD11B
298 (a marker for myeloid cells) co-staining on tumor slides of KP and EKP and observed
299 the relatively higher enrichment of MDSC markers in EKP (**Fig. 4O and 4U**). These
300 results suggest that CDH1 is a gatekeeper restricting the immune evasion of DGAC,
301 confirming immune landscape remodeling associated with the DGAC1 subtype where
302 CDH1 is inactivated.

303

304 ***Cdh1* depletion-activated EZH2 regulon promotes gastric tumorigenesis**

305 Since CDH1 loss is associated with distinct molecular signatures of DGAC1 (**Fig. 1M**),
306 we sought to identify key transcriptional regulatory modules (regulons) activated by
307 *Cdh1* depletion. We integrated the scRNA-seq datasets of WT, KP, and EKP into batch-
308 based and regulon pattern-based UMAPs (**Fig. 5A**). In the regulon activity-based
309 UMAP, six major transcriptional clusters (0~5) were identified (**Fig. 5A**). With the
310 separated UMAP, we observed that WT and KP shared somewhat similar
311 transcriptional landscape. However, EKP exhibited distinct features with an increased
312 cluster 5 (**Fig. 5B**). To pinpoint essential regulons, we created an unbiased workflow
313 (**Fig. 5C**). Based on the Z score of each regulon, we identified 32 regulons specific to
314 EKP transcriptional profile, compared to those of WT and KO (**Fig. 5D**). Additionally,
315 regulon specificity score (RSS) analysis showed the top 20 regulons specific to EKP
316 (**Fig. 5E**). RSS-based top 20 regulons belonged to Z score-based regulons (**Fig. 5F**,
317 **Table S18**). Both RSS and Z-score were used to quantify the activity of a gene or set of
318 genes. Z-score was used to quantify the level of gene expression in a particular sample,
319 while RSS was used to quantify the specificity of a gene set to a particular regulatory
320 network or module (Kelley et al., 2016). According to TCGA-based upregulation in
321 DGAC patients compared to normal stomach tissues, 13 regulons (Brca1, E2f1, E2f3,
322 E2f7, E2f8, Ezh2, Gabpa, Gtf2b, Gtf2f1, Hmga2, Pole4, Sox4, and Tfdp1) were selected
323 (**fig. S5A**). Next, we examined the regulons' expression in organoids datasets.
324 Compared to WT and KP, the expression of Ezh2, Gtf2b, Pole4, and Sox4 was
325 obviously increased in EKP GOs with over 40% fractions of clusters (**Fig. 5G**).
326 According to the regulon activity-based UMAP, Ezh2 displayed the highest score in EKP
327 compared to WT and KP GOs (**Fig. 5H**, **fig. S5B**). To assess the pathological relevance
328 of EZH2 to DGAC, we analyzed the expression of downstream target genes of EZH2 in
329 the DGAC datasets (**Table S9**) (Yu et al., 2023). One gene list included the genes
330 which are downregulated by EZH2 activation through histone modification
331 (EZH2_histone_modification_down) (**Fig. 5I**, **fig. S5C**, **Table S9**); the other gene list
332 included the genes which are downregulated by EZH2 activation that reported in gastric
333 cancer (EZH2_activation_down_in_GC) (**Fig. 5J**, **fig. S5D**, **Table S9**). Compared to
334 DGAC2 (CDH1 high), the EZH2_histone_modification_down and
335 EZH2_activation_down_in_GC scores were relatively lower in DGAC1 (CDH1 loss)
336 (**Fig. 5I**, **J**). EZH2 is a histone methyltransferase catalyzing the methylation of histone
337 H3 lysine 27 (H3K27) to generate H3K27me3, which is associated with gene repression
338 (Lee et al., 2007). Consistent with EZH2 regulon activation by *Cdh1* KO, H3K27Me3
339 was also increased in EKP tumors compared to KP, while no significant difference in
340 H3K27Ac expression (**Fig. 5K**). Next, we treated EKP cells with GSK343, a specific
341 inhibitor of EZH2 methyltransferase (Verma et al., 2012). EKP cells were more sensitive
342 to GSK343 than KP in cell proliferation in vitro (**Fig. 5L**). Meanwhile, we conducted
343 experiments to evaluate the effect of GSK343 on KP and EKP organoids (**Fig. 5M**). We
344 observed that the number of EKP GOs was significantly decreased (30.8%) after

345 GSK343 treatment, while the number of KP GOs was marginally affected by GSK343
346 (92.6%) of the organoids initially seeded (**Fig. 5N**). Additionally, allograft transplantation
347 experiments showed the growth inhibitory effect of GSK343 on EKP tumorigenesis (**Fig.**
348 **5O, P, Q**). These results identify EZH2 as a key regulon contributing to tumorigenesis of
349 CDH1 inactivation-associated DGAC.

350

351 **Discussion**

352 The impact of CDH1 loss on sporadic DGAC tumorigenesis remains unknown. Single-
353 cell transcriptomics-based unsupervised clustering identified two subtypes of DGAC:
354 DGAC1 (CDH1-negative or downregulated) and DGAC2 (CDH1-positive). Unlike
355 DGAC2 lacking ascites tumor cells-associated immunologic response, the DGAC1
356 subtype is enriched with exhausted T cells. Single-cell transcriptomics and
357 transplantation assays showed that *Cdh1* KO, in conjunction with *Trp53* KO and
358 *Kras*^{G12D}, induces accelerated tumorigenesis and immune evasion. Moreover, EZH2
359 regulon specifically activated by CDH1 loss promotes DGAC tumorigenesis.

360 Patient stratification is crucial for improving therapeutic efficacy. Despite several
361 studies classifying GAC patients (Ge et al., 2018; Fukamachi et al., 2019; Tong et al.,
362 2019; Kim et al., 2020; Wang et al., 2020), such subtyping did not consider single-cell
363 level cellular convolution, which might be insufficient to represent the full spectrum of
364 DGAC features. Our stratification approach was based on the high dimensional
365 transcriptional signatures at the single-cell level, immune cell profiling, and cellular
366 network, which may complement limitations from the bulk analyses and likely better
367 stratify DGAC patients. Indeed, our unsupervised subtyping by tumor cell transcriptome
368 well matched with distinct immune cell properties (**Fig. 2A-C**). Furthermore, the
369 application of CellChat and GSEA analysis led to the identification of T cell-related
370 immune profiling as the dominant feature in DGAC1 (**Fig. 2D-F, fig. S3A-F**).
371 Interestingly, T cell exhaustion and immune checkpoint-related genes were notably
372 enriched in DGAC1 compared to DGAC2 (**Fig. 2G-L**), confirmed by the transplantation
373 experiments (**Fig. 4**). These results strongly suggest that DGAC1 patients might benefit
374 from T cell-based ICIs, whereas DGAC2 patients might be ICI non-responders (**Fig. 2**).

375 Understanding the biology of cancer immune evasion is also imperative for
376 improving cancer treatment. To date, how DGAC tumor cells evade immune
377 surveillance remains elusive. Our transplantation assays showed that in conjunction
378 with *Trp53* KO and *Kras*^{G12D}, CDH1 loss is sufficient for immune evasion of DGAC (**Fig.**
379 **4**). In line with this, EKP allografts displayed increased expression of CD3, CD4,
380 PDCD1, TIM3, and LY6G (**Fig. 4J-U**), also identified as molecular signatures of DGAC1
381 (**Fig. 2G-O**). These tantalizing results suggest a new role of CDH1 in restricting the
382 immune evasion of tumor cells beyond its canonical role in cell-cell adhesion.

383 Tumors are immunogenically categorized into 'hot', 'altered-excluded', 'altered-
384 immunosuppressed' and 'cold' (Galon and Bruni, 2019). The terms 'hot' and 'cold'
385 describe T cell-infiltrated inflamed tumors and non-infiltrated tumors, respectively (Galon
386 et al., 2006). Altered-immunosuppressed tumors have few CD8+ T cells, mainly at the
387 tumor's periphery, with immune-suppressing cells like MDSCs and regulatory T cells. In
388 altered-excluded immune tumors, CD8+ T cells are absent, and the tumor
389 microenvironment is dense and hypoxic, hindering immune cell survival (Galon and

390 Bruni, 2019). Cold tumors, altered–immunosuppressed, or immune–excluded tumors,
391 respond less favorably to ICIs and generally have a poorer prognosis compared to hot
392 tumors, which tend to respond well to ICIs (Galon and Bruni, 2019; Lee and Ruppin,
393 2019). According to the immune profiling of EKP tumors (Fig. 4), which mimic DGAC1,
394 it is highly probable that DGAC1 may correspond to hot or altered–immunosuppressed
395 mixed tumors, while DGAC2 is likely to be classified as either cold tumors or altered–
396 excluded immune tumors. Emerging evidence suggests that *CDH1* loss may be
397 associated with an inflamed phenotype (Stodden et al., 2015; Kaneta et al., 2020). E-
398 Cadherin encoded by *CDH1* is an adhesion molecule responsible for maintaining cell-
399 cell interactions and tissue integrity. Loss of *CDH1* disrupts adherens junctions of tumor
400 cells and subsequently disorganizes tumor architecture (Bruner and Derksen, 2018),
401 which likely promotes immune cell infiltration.

402 Previously, two distinct molecular subtypes of GAC were introduced:
403 mesenchymal phenotype (MP) and epithelial phenotype (EP) (Oh et al., 2018; Wang et
404 al., 2020). Since its association with *CDH1* downregulation and EMT (fig. S1J), the
405 DGAC1 subtype might belong to the MP subtype, which displays poor survival and
406 chemotherapy resistance (Oh et al., 2018). Unlike DGAC1, DGAC2 does not show
407 *CDH1* loss and EMT. DGAC exhibits frequent mutations in the *TP53*, *CDH1*, *RHOA*,
408 *APC*, *CTNNB1*, *ARID1A*, *KMT2C*, and *PIK3CA* genes (Cancer Genome Atlas
409 Research, 2014; Kakiuchi et al., 2014; Oliveira et al., 2015; Cho et al., 2019). Among
410 these genes, *CDH1* and *RHOA* mutations are mainly observed in DGAC and not found
411 in IGAC (Cancer Genome Atlas Research, 2014; Kakiuchi et al., 2014; Cho et al.,
412 2019). As *CDH1* and *RHOA* both play a crucial role in modulating the cytoskeleton, cell
413 morphology, and cell migration (Handschoen et al., 1999; McBeath et al., 2004;
414 O'Connor and Chen, 2013; Al-Ahmadie et al., 2016), the general histological features of
415 DGAC are likely attributed to mutations in these genes, *CDH1* and *RHOA* (Ooki and
416 Yamaguchi, 2022). DGAC2 displays high *CDH1* expression and no EMT gene
417 expression (Fig. 1J-1L, fig. S1J). Additionally, DGAC2 shows *RHOA* signaling
418 activation (fig. S1N). Thus, epithelial cell polarity loss and the diffuse-type cell
419 (morphological) phenotype in DGAC2 might be due to *RHOA* mutations (Y42C) or
420 *RHOA* signaling activation, whereas *CDH1* loss is linked with DGAC1.

421 E-Cadherin mediates cell-cell interaction via homophilic interaction with other E-
422 Cadherin proteins from neighboring cells. The cytoplasmic domain of E-Cadherin is
423 physically associated with Catenin proteins (α , β , γ , and p120) and actin cytoskeleton,
424 which plays a pivotal role in maintaining epithelial cell polarity and integrity (McCrea and
425 Park, 2007). In our scRNA-seq study on EKP GOs, loss of *Cdh1* resulted in
426 transcriptional reprogramming and altered cell proportions, specifically reducing the
427 *Aqp5*^{high} cluster and increasing the *Mki67*^{high} cluster (Fig. 3J, K). *AQP5* is specifically
428 expressed in pyloric stem cells, as well as being frequently expressed in gastric cancers
429 and their metastases (Tan et al., 2020). Meanwhile, *Aqp5* was expressed in a
430 subpopulation of gastric cancer cells, some of which were *KI67*⁺. Our unbiased scRNA-
431 seq analysis distinctly revealed two separate clusters, namely *Aqp5*^{high} cells and

432 Mki67^{high} cells (**Fig. 3J**), denoting that the Aqp5^{high} cells within our murine GO model are
433 not proliferative. This finding aligns with Barker's study, wherein some Aqp5+ cells were
434 found to be Ki67 negative (Tan et al., 2020). Remarkably, in EKP organoids, we
435 observed a reduction in Aqp5^{high} cells alongside an increase in Mki67^{high} cells (**Fig. 3J, K**).
436 Consistently, in EKP tumors, a higher proportion of proliferative cells was observed
437 compared to KP tumors (**Fig. 4G, I**). These outcomes suggest that Mki67^{high} cells might
438 represent cells-of-origin in EKP tumors, characterizing the DGAC1 subtype with CDH1
439 loss. However, further rigorous experiments are warranted to validate this observation.

440 Intriguingly, CDH1 loss activates EZH2 regulon, and EZH2 blockade suppresses
441 EKP tumor growth (**Fig. 5**). EZH2 modulates gene expression in various ways: gene
442 repression via Polycomb Repressive Complex 2 (PRC2)-dependent histone
443 methylation, PRC2-dependent non-histone protein methylation, or gene activation via
444 transcriptional activator complex. The detailed mechanisms of how EZH2 is engaged in
445 CDH1 loss-associated DGAC tumorigenesis remain to be determined. Nonetheless,
446 given that an EZH2 inhibitor (tazemetostat) is clinically available, targeting EZH2 would
447 be a viable option for the DGAC1 subtype in addition to T cell-based ICIs. The use of
448 epigenetic modulators has been found to enhance the infiltration of effector T cells,
449 suppress tumor progression, and improve the therapeutic effectiveness of PD-L1
450 checkpoint blockade in prostate or head and neck cancer (Jadhav et al., 2019; Weber et
451 al., 2021). Additionally, pharmacological inhibition of EZH2 has been shown to inhibit
452 tumor growth and enhance the efficacy of anti-CTLA-4 treatment in bladder cancer
453 (Wherry and Kurachi, 2015). Given the enriched expression of immune checkpoints in
454 DGAC1 (**Fig. 2J-L**), a combination therapy involving EZH2 inhibitors and ICIs may hold
455 potential benefits for DGAC1 patients. Moreover, it should be determined whether
456 EZH2-induced transcriptional reprogramming mediates CDH1 loss-induced
457 transcriptional reprogramming of DGAC1.

458 Another remaining question is how CDH1 loss activates the EZH2 regulon.
459 Mesenchymal cells re-wire PI3K/AKT signaling to stimulate cell proliferation (Salt et al.,
460 2014). Additionally, it was shown that PI3K/AKT signaling is required for EZH2 activity in
461 KRAS^{G12D} mutant cells (Riquelme et al., 2016). Thus, it is plausible that EMT-activated
462 PI3K/AKT signaling might activate EZH2. Consistent with this, compared to DGAC2, the
463 DGAC1 subtype shows high scores for EMT and PI3K/AKT/MTOR pathways, and low
464 score for inversely related EZH2 downstream target gene expression (**fig. S1J, S1M**,
465 **Fig. 5I, J**).

466 Limitations of scRNA-seq include relatively shallow sequencing depth and
467 restricted information not overcoming intra-tumoral heterogeneity. Thus, increasing the
468 number of scRNA-seq datasets and spatial transcriptomics should follow in future
469 studies. Furthermore, although this is the first stratification of DGAC by single-cell
470 transcriptome, the pathological relevance of CDH1 status (or alternative molecular
471 signatures; **Fig. 1M**) with ICI response remains to be clinically demonstrated.

472 Together, our study stratifies DGAC patients by integrative single-cell
473 transcriptomics with experimental validation and unravels an unexpected role of CDH1
474 in restricting transcriptional reprogramming and immune evasion of DGAC, which
475 provides new insight into the biology of DGAC tumorigenesis and helps improve
476 immunotherapy efficacy.

477

478 **Author contributions**

479 G.Z., Y.H., and J.-I.P. conceived and designed the experiments. G.Z., Y.H., S.Z., K.-
480 P.K., B.K., J.Z., S.J., and V.V. performed the experiments. G.Z., Y.H., S.Z., K.-P.K.,
481 B.K., S.S., J.A.A., and J.-I.P. analyzed the data. M.P.P., Y.F., S.S., and J.A.A. provided
482 the sequencing files and clinical data for human scRNA-seq analyses. N.N. and H.W.
483 read and analyzed the stained slides. G.Z., Y.H., S.Z., K.-P.K., B.K., and J.-I.P. wrote
484 the manuscript.

485

486

487 **Acknowledgments**

488 We are grateful to Pierre D. McCrea, Malgorzata Kloc, Rachael Miller, and Adriana
489 Paulucci for their insightful comments. This work was supported by the Cancer
490 Prevention and Research Institute of Texas (RP200315 to J.-I.P.). The core facilities at
491 MD Anderson (DNA Sequencing and Genetically Engineered Mouse Facility) were
492 supported by National Cancer Institute Cancer Center Support Grant (P30 CA016672).
493 This work was performed at the Single Cell Genomics Core at BCM partially supported
494 by NIH-shared instrument grants (S10OD023469, S10OD025240) and P30EY002520.

495

496 **Methods**

497

498

499 **Mice**

500 All mouse experiments were approved by the MD Anderson Institutional Animal Care
501 and Use Committee and performed under MD Anderson guidelines and the Association
502 for Assessment and Accreditation of Laboratory Animal Care international standards.
503 Compound transgenic mice *Kras*^{LSL-G12D/+}; *Trp53*^{f/f} (KP) mice have been previously
504 described (Kim et al., 2021). C57BL/6 mice were purchased from the Jackson
505 Laboratory (Maine, USA).

506

507 **Gastric organoids generation**

508 The protocol for generating gastric organoids (GOs) was previously described (Bartfeld
509 et al., 2015). The mice were sacrificed, and the mouse stomach was collected, and the
510 forestomach was removed. Then, the reserved stomach tissue was cut through the
511 lesser curvature, and the stomach was rinsed with ice-cold PBS with 1%
512 penicillin/streptomycin to remove blood. The tissue samples were carefully immersed in
513 chelating buffer (sterile distilled water with 5.6 mmol/L Na₂HPO₄, 8.0 mmol/L KH₂PO₄,
514 96.2 mmol/L NaCl, 1.6 mmol/L KCl, 43.4 mmol/L sucrose, 54.9 mmol/L D-sorbitol, 0.5
515 mmol/L DL-dithiothreitol, pH 7) in a 10 cm dish, then the tissue was transferred to a dry
516 dish. The epithelial layer was peeled and minced into pieces using forceps. Minced
517 epithelial pieces were placed into 10 mL cold chelating buffer, followed by robust
518 pipetting up and down to rinse the tissue until the supernatant was clear. A 20 mL
519 chelating buffer was prepared with 10 mM EDTA under room temperature, and the
520 tissue was incubated in there for 10 min. The tissue was tenderly pipetted gently once
521 up and down, and the pieces were allowed to settle. The tissue was then moved to the
522 clean bench. Most of the water was removed, and the tissue pieces were carefully
523 placed in the middle of a sterile 10 cm dish. A glass microscopy slide was put on top of
524 the tissue and pressure was added upon the slide until the tissue pieces seemed
525 cloudy. The cloudy tissue pieces were then flushed from the slides in 30 mL of cold
526 Advanced DMEM/F12. The large tissue fragments were allowed to sediment by gravity.
527 The cloudy supernatant was transferred to two 15 ml tubes. The tubes were then
528 centrifuged for 5 min at 200 g and 4°C. The supernatant was carefully removed and
529 resuspended with Matrigel-medium mixture (12 µL Matrigel mix with 8 µL GOs culture
530 medium/well). Approximately 40 glands per 20 µL Matrigel-medium mixture per well of a
531 48-well plate were seeded. The plate was steadily transferred to the incubator to let it
532 solidify for 10 minutes. Then, 500 µL of GOs culture medium was added to cover the
533 dome, and the plate was incubated at 37 °C with 5% CO₂. The medium was changed
534 every 2 days.

535

536 **Gastric organoids culture**

537 **Table S1** was referred to for the culture medium ingredient. The organoids were
538 passaged using the following steps: **1.** The culture medium was discarded. **2.** The
539 Matrigel was scraped with a pipette tip and dissociated by pipetting. **3.** The organoids

540 were collected from three wells (48-well) in the 15 mL tube with cold medium. **4.** The
541 supernatant was discarded after centrifugation at 1000 RPM and 4°C. **5.** The
542 dissociated organoids were washed with 13 mL of cold 1× PBS, centrifuged (1000 RPM,
543 4 min), and the supernatant was removed. **6.** The organoids were resuspended in 1 mL
544 of Trypsin-EDTA (0.05%). **7.** The sample was transferred to a 1.7 mL Eppendorf tube,
545 then pipetted up and down. **8.** The sample was incubated in a 37 °C with 5% CO2
546 incubator for 30 min to 45 min. **9.** The tube was vibrated every 10 min. **10.** The organoid
547 structure was further broken down by pipetting up and down. **11.** The sample was
548 checked under the microscopy to ensure the organoids digested into cells. **12.** The
549 sample was passed through the 35 µm cell strainer. **13.** The Trypsin was inactivated
550 with 10% FBS medium and pipetted vigorously. **14.** The sample was collected in the 15
551 mL tube and centrifuged for 4 min at 1000 RPM. **15.** The supernatant was aspirated,
552 and the cells were resuspended with GOs culture medium. **16.** The cells were counted,
553 viability was checked, and the appropriate number of cells was calculated. **17.** Every 8
554 µL of cell suspension was mixed with 12 µL of Matrigel as a mixture and seeded in the
555 48-well plate. **18.** The plate was transferred to the incubator and allowed to solidify for
556 10 minutes. **19.** 500 µL of GOs culture medium was added to cover the dome and
557 incubated at 37 °C with 5% CO2. **20.** The medium was changed every 2 days.

558 The organoids were cryopreserved as follows: The organoids were dissociated
559 following above **organoid passaging (step1-15)** protocol. The cells were then added
560 with 10% volume of DMSO and transferred to the cryovials.

561 **CRISPR/Cas9-based gene knockout in GOs**

562 Knockout (KO) of *Cdh1* was performed by CRISPR/Cas9 genome editing using
563 pLentiCRISPRv2 (Addgene plasmid #52961) according to Zhang laboratory's protocol
564 (Ran et al., 2013). Five single guide RNA (sgRNA) targeting *Cdh1* were designed using
565 CRISPRick (<https://portals.broadinstitute.org/gppx/crispick/public>) and cloned into a
566 pLentiCRISPRv2-puro vector. An empty sgRNA vector was used as a negative control.
567 The five targeting sequences against *Cdh1* were: #1: 5'-ATGAT GAAAA CGCCA
568 ACGGG-3', #2: 5'-ACCCC CAAGT ACGTA CGCGG-3', #3: 5'-TTACC CTACA TACAC
569 TCTGG-3', #4: 5'-AGGGA CAAGA GACCC CTCAA-3', and #5: 5'-CCCTC CAAAT
570 CCGAT ACCTG-3'. sgRNA 1# (5'-ATGAT GAAAA CGCCA ACGGG-3') was
571 successfully knock out *Cdh1* in GOs. See **Table S2** for primer sequence to validate
572 *Cdh1* knockout efficiency.

573 **Lentivirus production and transduction**

574 The HEK293T cells were co-transfected with 5 µg of constructs, 5 µg of plasmid Δ8.2
575 (Plasmid #8455, Addgene), and 3 µg of plasmid VSVG (Plasmid #8454, Addgene) in a
576 10 cm dish. The cells were incubated at 37°C, and the medium was replaced after 12 h.
577 The virus-containing medium was collected 48 h after transfection. The organoids were
578 dissociated following the **organoid passaging protocol (step 1-14)**, and the
579 supernatant was aspirated, leaving the pellet. For transduction, 20 µL of cell suspension
580 was used. The amount of polybrene (8 µg/mL) was calculated and mixed with virus-
581 containing medium before adding to the cells. The polybrene containing virus medium
582
583

584 was added to the cell pellet, and the cell suspension was transferred to a 1.7 mL
585 Eppendorf Tube. The tube was centrifuged at 600 g at 37 °C for 1 h. Without disturbing
586 the cell pellet, the tube was incubated in the 37 °C incubator for 4 h. The supernatant
587 was then removed, and the cell pellet was resuspended with the required volume of
588 GOs culture medium (8 µL for one well of 48-well plate) and placed on ice for cool
589 down. The appropriate volume of pre-thawed Matrigel (12 µL for one well of 48-well
590 plate) was added to the tube, and the dome was seeded in the middle of a 48-well plate.
591 The plate was then incubated for 10 min at 37 °C with 5% CO₂. GOs culture medium
592 was added to the well. After 48 h, the infected organoids were selected with 1 µg/mL
593 puromycin.

594

595 **Adenovirus transduction**

596 We used Adeno-Cre virus to treat *Kras*^{LSL-G12D/+}; *Trp53*^{fl/fl} organoids. The protocol was
597 previously described (Ko et al., 2022; Ko et al., 2023). The cells were first dissociated
598 from GOs as described in the **organoid passaging protocol (step 1-14)**. The cell
599 number was counted, and the ratio of adenovirus: organoid cell was 1000 PFU/µL:1
600 cell. The cell suspension, virus-containing medium, and Matrigel were mixed, and the
601 drop was placed in the center of the well. The cell suspension and virus-containing
602 medium were mixed before adding GOs culture medium up to 8 µL. Then, 12 µL of
603 Matrigel was added to the mixture on ice. The plate was incubated in the 37°C cell
604 culture incubator for 15 min to allow the Matrigel to solidify. After 48 h, the infected
605 organoids were treated with 10 µM Nutlin-3 to select *Trp53* KO organoids. The primer
606 sequence to validate *Trp53* KO and *Kras*^{G12D/+} can be found in **Table S2**.

607

608 **Organoid imaging and size measurement**

609 After 7 days of organoid seeding in Matrigel, the size of the organoids was analyzed by
610 measuring the volume under the microscope (ZEN software, ZEISS). To reduce the
611 vulnerability of GOs, the measurements were conducted more than 3 passages after
612 isolation from the knockout experiments. All experiments included more than 50
613 organoids per group.

614

615 **Tissue microarray**

616 DGAC cancer tissue microarray slides contained 114 patients' samples. Patients'
617 information is shown in **Table S4**.

618

619 **Histology and immunohistochemistry**

620 All staining was performed as previously described (Jung et al., 2018). For organoids
621 staining, 7 days after seeding, GOs were collected by dissociating Matrigel mixture
622 using ice-cold PBS and fixed in 4% paraformaldehyde at room temperature. For tumor
623 tissue, excised tumors were washed with ice-cold PBS and fixed with formaldehyde at
624 room temperature. After paraffin embedding, tumor tissue and organoid sections were
625 mounted on microscope slides. For H&E staining, sections were incubated in
626 hematoxylin for 3-5 min and eosin for 20-40 s. After washing with tap water, slides were
627 dehydrated, and the coverslips were mounted with mounting media. For

628 immunofluorescence staining, after blocking with 5% goat serum in PBS for 1 hr at room
629 temperature, sections were incubated with primary antibodies (MKI67 [1:200], CDH1
630 [1:200], CD3 [1:200], CD8 [1:200], CD4 [1:200], PDCD1 [1:200], TIM3 [1:200], CD11B
631 [1:200], LY6G [1:200]) overnight at 4 °C and secondary antibody (1:250) for 1 hr at
632 room temperature in dark. Sections were mounted with ProLong Gold antifade reagent
633 with DAPI (Invitrogen). For immunohistochemistry staining, after blocking with 5% goat
634 serum in PBS for 1 hr at room temperature, sections were incubated with primary
635 antibodies (CDH1 [1:200], H3K27Me3 [1:200], H3K27Ac [1:200]) overnight at 4 °C and
636 secondary antibody (1:250) for 1 hr at room temperature in dark. Incubate the slides in
637 the DAB solution until tissue become brown and background still white. Observed under
638 the microscope until the strongest signal shows and stop reaction with tap water wash.
639 Used the same incubation time for same antibody on different slides. Sections were
640 incubated in hematoxylin for 3-5 min and mounted with mounting media. Images were
641 captured with the fluorescence microscope (Zeiss; AxioVision). See **Table S3** for
642 antibody information.

643

644 **2D culture**

645 The organoids were dissociated following the **organoid passaging protocol (step1-14)**. The supernatant was aspirated and then resuspended with DMEM + 10% FBS with
646 10 µM Y-27632, and the organoids were seeded on a 24-well plate. Cells were
647 passaged every 3-5 days. After the third passage, Y-27632 was removed from the
648 culture medium. DMEM supplemented with 10% FBS and 10% DMSO was used to
649 freeze cells and store them in liquid nitrogen.

650

651 **Allograft transplantation**

652 Five-week-old C57BL/6 mice were maintained in the Division of Laboratory Animal
653 Resources facility at MD Anderson. 2D-cultured KP and EKP cells (1×10^6) were
654 injected subcutaneously into both flanks of mice. Tumor volume was calculated by
655 measuring with calipers every 3-4 days (volume = (length \times width²)/2). Mice were
656 euthanized, and tumors were collected at day 15. The excised tumors were
657 photographed and paraffin-embedded for immunostaining. For GSK343 treatment, 2D-
658 cultured EKP cells (1×10^6) were injected subcutaneously into both flanks of mice. After
659 the tumors were palpable, we performed the first measurement with calipers. We
660 divided the mice into two groups of three mice each and administered DMSO and
661 GSK343 (20 mg/kg) intraperitoneally every other day. The initial tumor volumes
662 between the two groups were comparable. Tumor volume was calculated by measuring
663 with calipers every 3-4 days (volume = (length \times width²)/2). Mice were euthanized, and
664 tumors were collected at day 20.

665

666 **Crystal violet staining**

667 Cells (1×10^3) were seeded on a 6-well plates, and the medium was replaced every 2
668 days. Plates were rinsed with 1× PBS, fixed with 4% paraformaldehyde solution for 20
669 min, and stained with crystal violet solution (0.1% crystal violet, 10% methanol) for 20
670 min, followed by rinsing with tap water.

671

672

673 **Gastric organoids library preparation for scRNA-seq**

674 For scRNA-seq, organoids from WT, KP, and EKP were collected 7 days after seeding
675 and follow the **organoid passaging (step1-14)** protocol. After trypsin had been
676 inactivated with 10% FBS DMEM, a single-cell suspension was collected by passing
677 cells through a 70 μ m cell strainer and followed by a 40 μ m cell strainer. Each group
678 was tagged with two CMO tags from the CellPlex kit (10x Genomics). The tagged cells
679 of each group were pooled together with the same number of cells after being counted.
680 Single cell Gene Expression Library was prepared according to Chromium Single Cell
681 Gene Expression 3v3.1 kit with Feature Barcode technology for cell Multiplexing (10x
682 Genomics). In brief, tagged single cells, reverse transcription (RT) reagents, Gel Beads
683 containing barcoded oligonucleotides, and oil were loaded on a Chromium controller
684 (10x Genomics) to generate single cell GEMS (Gel Beads-In-Emulsions). Incubation of
685 the GEM produced barcoded, full-length cDNA as well as barcoded DNA from the cell
686 Multiplexing. Subsequently the GEMS are broken and pooled. Following cleanup using
687 Dynabeads MyOne Silane Beads, full-length cDNA is amplified by PCR for library prep
688 through fragmentation, end-repair, A-tailing, adaptor ligation and amplification, while the
689 barcoded DNA from the cell Multiplexing is amplified for library prep via PCR to add
690 sequencing primers. The cDNA library was sequenced on an Illumina NovaSeq platform
691 (Novogene), mapped to the GRCm38/mm10 genome, and demultiplexed using
692 CellRanger. The resulting count matrices files were analyzed in R (Seurat) or Python
693 (Scanpy).

694

695 **scRNA-seq - raw data processing, clustering, and annotation**

696 We used Cell Ranger to perform demultiplexing and reads alignment of sequencing raw
697 data for the scRNA-seq matrices generation. Ambient RNA and doublets were removed
698 by SoupX (Young and Behjati, 2020) and Scrublet (Wolock et al., 2019), respectively.
699 Scanpy(Wolf et al., 2018) was used for processing the scRNA-seq data. For the
700 organoid dataset, cells with less than 50 genes expressed and more than 30%
701 mitochondrial reads, 30% rpl reads, and 25% rps reads were removed. Genes
702 expressed in less than 5 cells were removed. Then we normalized and log-transformed
703 the gene expression for each cell. The percentages of mitochondrial reads, rpl reads,
704 and rps reads were regressed before scaling the data. We reduced dimensionality and
705 cluster the cells by Leiden (resolution=0.5). Cell lineages were annotated based on
706 algorithmically defined marker gene expression for each cluster
(sc.tl.rank_genes_groups, method='t-test'). See **Table S17**, the most differentially
707 expressed 100 genes of each cluster were listed. For the DGAC dataset, cells with less
708 than 100 genes expressed and more than 80% mitochondrial reads, 30% rpl reads, and
709 25% rps reads were removed. Genes expressed in less than 25 cells were removed.
710 Normalization, log-transformation, regression, dimensionality reduction, and Leiden
711 clustering (resolution=1) were the same as the way we use in organoids. Cell lineages
712 were annotated based on algorithmically defined marker gene expression for each
713 cluster (sc.tl.rank_genes_groups, method='t-test'). See **Table S6, S7, and S8** for
714 details, the most differentially expressed 100 genes of each cluster or type were listed.
715

716 For the DGAC dataset merged with normal stomach dataset, cells with less than 100
717 genes expressed and more than 100% mitochondrial reads, 40% rpl reads, and 30%
718 rps reads were removed. Genes expressed in less than 25 cells were removed.
719 Normalization, log-transformation, regression, dimensionality reduction, and Leiden
720 clustering (resolution=1) were the same as the way we use in organoids. Cell lineages
721 were annotated based on algorithmically defined marker gene expression for each
722 cluster (sc.tl.rank_genes_groups, method='t-test'). See **Table S10** for details, the most
723 differentially expressed 100 genes of each cluster were listed. More information about
724 the software and algorithms used in this study is shown in **Table S19**.
725

726 **Proportion difference analysis**

727 The cell number of each cluster were retrieved by Scanpy
728 (adata.obs['leiden'].value_counts()). We analyzed and plotted the differences between
729 clusters from the two datasets using the GraphPad Prism 9.4. Then we grouped each
730 cell cluster from the integrated dataset and compared the cluster differences between
731 the two datasets.

732 **Regulon analysis**

733 For the gene regulatory network inference in organoids, we used the pySCENIC
734 package (Van de Sande et al., 2020) to compute the specific regulons for each cell
735 cluster. The Loom file of each organoid dataset was used, and the regulon pattern-
736 based UMAP was redrawn based on the AUCell scoring method (Aibar et al., 2017).
737 Regulon specificity score (RSS) (Suo et al., 2018) and Z score were used to determine
738 how specific the regulon is for one certain cell cluster. More specific the regulon is, the
739 higher RSS or Z score is for one certain cluster. Following the criteria that RSS and Z
740 score should be high at the same time, we identified 20 regulons that specific to EKP.
741 These processes were repeated five times in each organoid dataset (WT, KP, and
742 EKP). RSS of regulons from each mouse gastric organoid dataset (WT, KP, and EKP)
743 was listed in **Table S18**.
744

745 **Scissor analysis**

746 To determine the pathology of murine organoids, we compared the transcriptomic
747 similarity of the organoids scRNA-seq dataset and the bulk RNA-seq datasets of DGAC
748 patients by Scissor package (Sun et al., 2022). The RNA-seq data of tumor and the
749 adjacent normal samples of DGAC patients were downloaded from the GDC data portal
750 (TCGA-STAD). The murine genes were converted to human homologs by biomaRt. The
751 Scissor analysis was performed by using the Cox regression model (alpha = 0.32). The
752 goal of Scissor is to identify a small group of cells that are most highly correlated with
753 the specific phenotypes with high confidence. Based on this motivation as a priori, we
754 determined α using the following criteria: the number of Scissor-selected cells should
755 not exceed a certain percentage of total cells (default 20%) in the single-cell data (Sun
756 et al., 2022).
757

758 **Cell-cell communication analysis**

760 'CellChat' (Jin et al., 2021) package in R (<https://www.r-project.org>) was used to
761 analysis the ligand-receptor interaction-based cell-cell communication in scRNA-seq
762 datasets. The integrated dataset was processed, clustered, and annotated using the
763 scanpy package (Wolf et al., 2018) in python, then transformed into .rds files.
764 Transformed datasets were analyzed by CellChat with default parameters (p-value
765 threshold = 0.05).

767 **Pathway score analysis**

768 Pathway score was analyzed by Scanpy (Wolf et al., 2018) with the
769 'scanpy.tl.score_genes' function (Wolf et al., 2018). The analysis was performed with
770 default parameters and the reference genes from the gene ontology biological process
771 or the Kyoto Encyclopedia of Genes and Genomes database (Kanehisa, 1996;
772 Ashburner et al., 2000). The gene list for the score analysis is shown in **Table S9**.

774 **Human scRNA-seq data analysis**

775 The scRNA-seq data set of 19 DGAC patients' samples (Patients information is shown
776 in **Table S5**) has been previous reported from our group and the detailed clinical and
777 histopathological characteristics are described (EGAS00001004443) (Wang et al.,
778 2021). The meta data of the scRNAseq is presented on **Table S5**.

779 The scRNA-seq data set of the 29 normal adjacent stomachs (GSE150290) (Kim
780 et al., 2022) was extracted from the Gene Expression Omnibus (GEO) database and
781 analyzed with Scanpy and Python (Wolf et al., 2018). The 19 DGAC patients' datasets
782 were integrated and clustered by Scanpy (Wolf et al., 2018) for the subclassification of
783 DGACs based on CDH1 inactivation. The 19 DGAC patients' datasets and 29 normal
784 adjacent stomachs were integrated and clustered in Scanpy (Wolf et al., 2018) for later
785 infercnvpy analysis. "Harmony" (Korsunsky et al., 2019) algorithm was used to remove
786 batch effects. Then, the dendrogram and correlation matrix heatmap were plotted with
787 Scanpy (Wolf et al., 2018). The dendrogram shows the distance of each dataset based
788 on principal component analysis, and the correlation matrix heatmap shows Pearson
789 correlation by a color spectrum.

791 **Copy number variation analysis**

792 To detect the genomic stability of groups DGAC1, DGAC2, we performed copy number
793 variations (CNVs) inference from the gene expression data using the Python package
794 infercnvpy (<https://icbi-lab.github.io/infercnvpy/index.html>). We performed infercnvpy on
795 DGAC1, DGAC2 using the Normal group (29 human normal adjacent stomachs) as
796 reference. The gene ordering file which is containing the chromosomal start and end
797 position for each gene was created from the human GRCh38 assembly. The GRCh38
798 genomic positions annotated file was downloaded from
<https://support.10xgenomics.com/single-cell-gene-expression/software/downloads/latest>. Infercnvpy was used to plot chromosome
800 heatmap and CNV scores in the UMAP.

803 **Gene set enrichment analysis (GSEA)**

804 GSEA was conducted via the R package “fgsea” (Korotkevich et al., 2021) according to
805 the DEG list generated by Scanpy. NES (Normalized Enrichment Score) represents the
806 degree of enrichment of a gene set in a given dataset, measuring the coordinated
807 upregulation or downregulation of genes within the set compared to a reference
808 condition. It is normalized to account for variations in gene set size and dataset
809 characteristics, providing a more robust measure of enrichment. The enrichment value
810 was calculated and plotted with the fgsea package (permutation number = 2,000). All
811 enriched pathways were listed in **Table S11-S16**.

812
813 **Public sequencing database**
814 All TCGA cancer patients' sequencing data referenced in this study were obtained from
815 the TCGA database at cBioPortal Cancer Genomics (<http://www.cbioportal.org>).
816

817 **Data availability**
818 scRNA-seq data are available via the GEO database (GSE226266; log-in token for
819 reviewers: edazwaukzvsxbop).
820

821 **Code availability**
822 The code used to reproduce the analyses described in this manuscript can be accessed
823 via GitHub (https://github.com/jaeilparklab/EKP_DGAC_project) and will also be
824 available upon request.
825

826 **Statistical analyses**
827 GraphPad Prism 9.4 (Dogmatics) was used for statistical analyses. The Student's *t*-test
828 was used to compare two samples. The one-way ANOVA was used to compare multiple
829 samples. *P* values < 0.05 were considered statistically significant. Error bars indicate
830 the standard deviation (s.d.) otherwise described in figure legends.
831

832

833 **References**

834 Aibar, S., C. B. Gonzalez-Blas, T. Moerman, V. A. Huynh-Thu, H. Imrichova, G.
835 Hulselmans, F. Rambow, J. C. Marine, P. Geurts, J. Aerts, J. van den Oord, Z. K. Atak,
836 J. Wouters and S. Aerts. 2017. SCENIC: single-cell regulatory network inference and
837 clustering. *Nat Methods* 14: 1083-1086.

838 Ajani, J. A., T. A. D'Amico, D. J. Bentrem, J. Chao, D. Cooke, C. Corvera, P. Das, P. C.
839 Enzinger, T. Enzler, P. Fanta, F. Farjah, H. Gerdes, M. K. Gibson, S. Hochwald, W. L.
840 Hofstetter, D. H. Ilson, R. N. Keswani, S. Kim, L. R. Kleinberg, S. J. Klempner, J. Lacy,
841 Q. P. Ly, K. A. Matkowskyj, M. McNamara, M. F. Mulcahy, D. Outlaw, H. Park, K. A.
842 Perry, J. Pimiento, G. A. Poultides, S. Reznik, R. E. Roses, V. E. Strong, S. Su, H. L.
843 Wang, G. Wiesner, C. G. Willett, D. Yakoub, H. Yoon, N. McMillian and L. A. Pluchino.
844 2022. Gastric Cancer, Version 2.2022, NCCN Clinical Practice Guidelines in Oncology.
845 *J Natl Compr Canc Netw* 20: 167-192.

846 Al-Ahmadie, H. A., G. Iyer, B. H. Lee, S. N. Scott, R. Mehra, A. Bagrodia, E. J. Jordan,
847 S. P. Gao, R. Ramirez, E. K. Cha, N. B. Desai, E. C. Zabor, I. Ostrovnaya, A. Gopalan,
848 Y. B. Chen, S. W. Fine, S. K. Tickoo, A. Gandhi, J. Hreiki, A. Viale, M. E. Arcila, G.
849 Dalbagni, J. E. Rosenberg, B. H. Bochner, D. F. Bajorin, M. F. Berger, V. E. Reuter, B.
850 S. Taylor and D. B. Solit. 2016. Frequent somatic CDH1 loss-of-function mutations in
851 plasmacytoid variant bladder cancer. *Nat Genet* 48: 356-358.

852 Ashburner, M., C. A. Ball, J. A. Blake, D. Botstein, H. Butler, J. M. Cherry, A. P. Davis,
853 K. Dolinski, S. S. Dwight, J. T. Eppig, M. A. Harris, D. P. Hill, L. Issel-Tarver, A.
854 Kasarskis, S. Lewis, J. C. Matese, J. E. Richardson, M. Ringwald, G. M. Rubin and G.
855 Sherlock. 2000. Gene ontology: tool for the unification of biology. The Gene Ontology
856 Consortium. *Nat Genet* 25: 25-29.

857 Assumpcao, P. P., W. F. Barra, G. Ishak, L. G. V. Coelho, F. J. F. Coimbra, H. C.
858 Freitas, E. Dias-Neto, M. C. Camargo and M. Szklo. 2020. The diffuse-type gastric
859 cancer epidemiology enigma. *BMC Gastroenterol* 20: 223.

860 Bartfeld, S., T. Bayram, M. van de Wetering, M. Huch, H. Begthel, P. Kujala, R. Vries, P.
861 J. Peters and H. Clevers. 2015. In vitro expansion of human gastric epithelial stem cells
862 and their responses to bacterial infection. *Gastroenterology* 148: 126-136 e126.

863 Blair, V. R., M. McLeod, F. Carneiro, D. G. Coit, J. L. D'Addario, J. M. van Dieren, K. L.
864 Harris, N. Hoogerbrugge, C. Oliveira, R. S. van der Post, J. Arnold, P. R. Benusiglio, T.
865 M. Bisseling, A. Boussioutas, A. Cats, A. Charlton, K. E. C. Schreiber, J. L. Davis, M. D.
866 Pietro, R. C. Fitzgerald, J. M. Ford, K. Gamet, I. Gullo, R. H. Hardwick, D. G.
867 Huntsman, P. Kaurah, S. S. Kupfer, A. Latchford, P. F. Mansfield, T. Nakajima, S. Parry,
868 J. Rossaak, H. Sugimura, M. Svrcek, M. Tischkowitz, T. Ushijima, H. Yamada, H. K.
869 Yang, A. Claydon, J. Figueiredo, K. Paringatai, R. Seruca, N. Bougen-Zhukov, T. Brew,
870 S. Busija, P. Carneiro, L. DeGregorio, H. Fisher, E. Gardner, T. D. Godwin, K. N. Holm,

871 B. Humar, C. J. Lintott, E. C. Monroe, M. D. Muller, E. Norero, Y. Nouri, J. Paredes, J.
872 M. Sanches, E. Schulpen, A. S. Ribeiro, A. Sporle, J. Whitworth, L. Zhang, A. E. Reeve
873 and P. Guilford. 2020. Hereditary diffuse gastric cancer: updated clinical practice
874 guidelines. *Lancet Oncol* 21: e386-e397.

875 Boku, N., T. Satoh, M. H. Ryu, Y. Chao, K. Kato, H. C. Chung, J. S. Chen, K. Muro, W.
876 K. Kang, K. H. Yeh, T. Yoshikawa, S. C. Oh, L. Y. Bai, T. Tamura, K. W. Lee, Y.
877 Hamamoto, J. G. Kim, K. Chin, D. Y. Oh, K. Minashi, J. Y. Cho, M. Tsuda, T.
878 Nishiyama, L. T. Chen and Y. K. Kang. 2021. Nivolumab in previously treated advanced
879 gastric cancer (ATTRACTION-2): 3-year update and outcome of treatment beyond
880 progression with nivolumab. *Gastric Cancer* 24: 946-958.

881 Bruner, H. C. and P. W. B. Derkisen. 2018. Loss of E-Cadherin-Dependent Cell-Cell
882 Adhesion and the Development and Progression of Cancer. *Cold Spring Harb Perspect
883 Biol* 10.

884 Cancer Genome Atlas Research, N. 2014. Comprehensive molecular characterization
885 of gastric adenocarcinoma. *Nature* 513: 202-209.

886 Chen, Y. C., W. L. Fang, R. F. Wang, C. A. Liu, M. H. Yang, S. S. Lo, C. W. Wu, A. F. Li,
887 Y. M. Shyr and K. H. Huang. 2016. Clinicopathological Variation of Lauren
888 Classification in Gastric Cancer. *Pathol Oncol Res* 22: 197-202.

889 Cho, J., S. Ahn, D. S. Son, N. K. Kim, K. W. Lee, S. Kim, J. Lee, S. H. Park, J. O. Park,
890 W. K. Kang, J. Y. An, M. G. Choi, J. H. Lee, T. S. Sohn, J. M. Bae, S. Kim and K. M.
891 Kim. 2019. Bridging genomics and phenomics of gastric carcinoma. *Int J Cancer* 145:
892 2407-2417.

893 Cristescu, R., J. Lee, M. Nebozhyn, K. M. Kim, J. C. Ting, S. S. Wong, J. Liu, Y. G. Yue,
894 J. Wang, K. Yu, X. S. Ye, I. G. Do, S. Liu, L. Gong, J. Fu, J. G. Jin, M. G. Choi, T. S.
895 Sohn, J. H. Lee, J. M. Bae, S. T. Kim, S. H. Park, I. Sohn, S. H. Jung, P. Tan, R. Chen,
896 J. Hardwick, W. K. Kang, M. Ayers, D. Hongyue, C. Reinhard, A. Loboda, S. Kim and A.
897 Aggarwal. 2015. Molecular analysis of gastric cancer identifies subtypes associated
898 with distinct clinical outcomes. *Nat Med* 21: 449-456.

899 Fukamachi, H., S. K. Kim, J. Koh, H. S. Lee, Y. Sasaki, K. Yamashita, T. Nishikawaji, S.
900 Shimada, Y. Akiyama, S. J. Byeon, D. H. Bae, K. Okuno, M. Nakagawa, T. Tanioka, M.
901 Inokuchi, H. Kawachi, K. Tsuchiya, K. Kojima, T. Tokino, Y. Eishi, Y. S. Kim, W. H. Kim,
902 Y. Yuasa and S. Tanaka. 2019. A subset of diffuse-type gastric cancer is susceptible to
903 mTOR inhibitors and checkpoint inhibitors. *J Exp Clin Cancer Res* 38: 127.

904 Galon, J. and D. Bruni. 2019. Approaches to treat immune hot, altered and cold
905 tumours with combination immunotherapies. *Nat Rev Drug Discov* 18: 197-218.

906 Galon, J., A. Costes, F. Sanchez-Cabo, A. Kirilovsky, B. Mlecnik, C. Lagorce-Pages, M.
907 Tosolini, M. Camus, A. Berger, P. Wind, F. Zinzindohoue, P. Bruneval, P. H. Cugnenc,

908 Z. Trajanoski, W. H. Fridman and F. Pages. 2006. Type, density, and location of
909 immune cells within human colorectal tumors predict clinical outcome. *Science* 313:
910 1960-1964.

911 Garcia-Pelaez, J., R. Barbosa-Matos, I. Gullo, F. Carneiro and C. Oliveira. 2021.
912 Histological and mutational profile of diffuse gastric cancer: current knowledge and
913 future challenges. *Mol Oncol* 15: 2841-2867.

914 Ge, S., X. Xia, C. Ding, B. Zhen, Q. Zhou, J. Feng, J. Yuan, R. Chen, Y. Li, Z. Ge, J. Ji,
915 L. Zhang, J. Wang, Z. Li, Y. Lai, Y. Hu, Y. Li, Y. Li, J. Gao, L. Chen, J. Xu, C. Zhang, S.
916 Y. Jung, J. M. Choi, A. Jain, M. Liu, L. Song, W. Liu, G. Guo, T. Gong, Y. Huang, Y.
917 Qiu, W. Huang, T. Shi, W. Zhu, Y. Wang, F. He, L. Shen and J. Qin. 2018. A proteomic
918 landscape of diffuse-type gastric cancer. *Nat Commun* 9: 1012.

919 Handschuh, G., S. Candidus, B. Luber, U. Reich, C. Schott, S. Oswald, H. Becke, P.
920 Hutzler, W. Birchmeier, H. Hofler and K. F. Becker. 1999. Tumour-associated E-
921 cadherin mutations alter cellular morphology, decrease cellular adhesion and increase
922 cellular motility. *Oncogene* 18: 4301-4312.

923 Hayakawa, Y., H. Ariyama, J. Stancikova, K. Sakitani, S. Asfaha, B. W. Renz, Z. A.
924 Dubeykovskaya, W. Shibata, H. Wang, C. B. Westphalen, X. Chen, Y. Takemoto, W.
925 Kim, S. S. Khurana, Y. Tailor, K. Nagar, H. Tomita, A. Hara, A. R. Sepulveda, W. Setlik,
926 M. D. Gershon, S. Saha, L. Ding, Z. Shen, J. G. Fox, R. A. Friedman, S. F. Konieczny,
927 D. L. Worthley, V. Korinek and T. C. Wang. 2015. Mist1 Expressing Gastric Stem Cells
928 Maintain the Normal and Neoplastic Gastric Epithelium and Are Supported by a
929 Perivascular Stem Cell Niche. *Cancer Cell* 28: 800-814.

930 Henson, D. E., C. Dittus, M. Younes, H. Nguyen and J. Albores-Saavedra. 2004.
931 Differential trends in the intestinal and diffuse types of gastric carcinoma in the United
932 States, 1973-2000: increase in the signet ring cell type. *Arch Pathol Lab Med* 128: 765-
933 770.

934 Iyer, P., M. Moslim, J. M. Farma and C. S. Denlinger. 2020. Diffuse gastric cancer:
935 histologic, molecular, and genetic basis of disease. *Transl Gastroenterol Hepatol* 5: 52.

936 Jadhav, R. R., S. J. Im, B. Hu, M. Hashimoto, P. Li, J. X. Lin, W. J. Leonard, W. J.
937 Greenleaf, R. Ahmed and J. J. Goronzy. 2019. Epigenetic signature of PD-1+ TCF1+
938 CD8 T cells that act as resource cells during chronic viral infection and respond to PD-
939 1 blockade. *Proc Natl Acad Sci U S A* 116: 14113-14118.

940 Janjigian, Y. Y., K. Shitara, M. Moehler, M. Garrido, P. Salman, L. Shen, L. Wyrwicz, K.
941 Yamaguchi, T. Skoczyłas, A. Campos Bragagnoli, T. Liu, M. Schenker, P. Yanez, M.
942 Tehfe, R. Kowalyszyn, M. V. Karamouzis, R. Bruges, T. Zander, R. Pazo-Cid, E. Hitre,
943 K. Feeney, J. M. Cleary, V. Poulart, D. Cullen, M. Lei, H. Xiao, K. Kondo, M. Li and J. A.
944 Ajani. 2021. First-line nivolumab plus chemotherapy versus chemotherapy alone for

945 advanced gastric, gastro-oesophageal junction, and oesophageal adenocarcinoma
946 (CheckMate 649): a randomised, open-label, phase 3 trial. *Lancet* 398: 27-40.

947 Jin, S., C. F. Guerrero-Juarez, L. Zhang, I. Chang, R. Ramos, C.-H. Kuan, P. Myung, M.
948 V. Plikus and Q. Nie. 2021. Inference and analysis of cell-cell communication using
949 CellChat. *Nature communications* 12: 1-20.

950 Jin, S., C. F. Guerrero-Juarez, L. Zhang, I. Chang, R. Ramos, C. H. Kuan, P. Myung, M.
951 V. Plikus and Q. Nie. 2021. Inference and analysis of cell-cell communication using
952 CellChat. *Nat Commun* 12: 1088.

953 Jung, Y. S., W. Wang, S. Jun, J. Zhang, M. Srivastava, M. J. Kim, E. M. Lien, J. Shang,
954 J. Chen, P. D. McCrea, S. Zhang and J. I. Park. 2018. Dereulation of CRAD-controlled
955 cytoskeleton initiates mucinous colorectal cancer via beta-catenin. *Nat Cell Biol* 20:
956 1303-1314.

957 Kakiuchi, M., T. Nishizawa, H. Ueda, K. Gotoh, A. Tanaka, A. Hayashi, S. Yamamoto,
958 K. Tatsuno, H. Katoh, Y. Watanabe, T. Ichimura, T. Ushiku, S. Funahashi, K. Tateishi, I.
959 Wada, N. Shimizu, S. Nomura, K. Koike, Y. Seto, M. Fukayama, H. Aburatani and S.
960 Ishikawa. 2014. Recurrent gain-of-function mutations of RHOA in diffuse-type gastric
961 carcinoma. *Nat Genet* 46: 583-587.

962 Kanehisa, M. 1996. Toward pathway engineering: a new database of genetic and
963 molecular pathways. *Sci. Technol. Jap.* 59: 34-38.

964 Kaneta, Y., T. Sato, Y. Hikiba, M. Sugimori, S. Sue, H. Kaneko, K. Irie, T. Sasaki, M.
965 Kondo, M. Chuma, W. Shibata and S. Maeda. 2020. Loss of Pancreatic E-Cadherin
966 Causes Pancreatitis-Like Changes and Contributes to Carcinogenesis. *Cell Mol
967 Gastroenterol Hepatol* 9: 105-119.

968 Kelley, D. R., J. Snoek and J. L. Rinn. 2016. Basset: learning the regulatory code of the
969 accessible genome with deep convolutional neural networks. *Genome Res* 26: 990-
970 999.

971 Kim, J., C. Park, K. H. Kim, E. H. Kim, H. Kim, J. K. Woo, J. K. Seong, K. T. Nam, Y. C.
972 Lee and S. Y. Cho. 2022. Single-cell analysis of gastric pre-cancerous and cancer
973 lesions reveals cell lineage diversity and intratumoral heterogeneity. *NPJ Precis Oncol*
974 6: 9.

975 Kim, M. J., C. Cervantes, Y. S. Jung, X. Zhang, J. Zhang, S. H. Lee, S. Jun, L.
976 Litovchick, W. Wang, J. Chen, B. Fang and J. I. Park. 2021. PAF remodels the DREAM
977 complex to bypass cell quiescence and promote lung tumorigenesis. *Mol Cell* 81:
978 1698-1714 e1696.

979 Kim, S. K., H. J. Kim, J. L. Park, H. Heo, S. Y. Kim, S. I. Lee, K. S. Song, W. H. Kim and
980 Y. S. Kim. 2020. Identification of a molecular signature of prognostic subtypes in
981 diffuse-type gastric cancer. *Gastric Cancer* 23: 473-482.

982 Ko, K. P., Y. Huang, S. Zhang, G. Zou, B. Kim, J. Zhang, S. Jun, C. Martin, K. J.
983 Dunbar, G. Efe, A. K. Rustgi, H. Nakagawa and J. I. Park. 2023. Key Genetic
984 Determinants Driving Esophageal Squamous Cell Carcinoma Initiation and Immune
985 Evasion. *Gastroenterology* 165: 613-628 e620.

986 Ko, K. P., J. Zhang and J. I. Park. 2022. Establishing transgenic murine esophageal
987 organoids. *STAR Protoc* 3: 101317.

988 Korfer, J., F. Lordick and U. T. Hacker. 2021. Molecular Targets for Gastric Cancer
989 Treatment and Future Perspectives from a Clinical and Translational Point of View.
990 *Cancers (Basel)* 13.

991 Korotkevich, G., V. Sukhov, N. Budin, B. Shpak, M. N. Artyomov and A. Sergushichev.
992 2021. Fast gene set enrichment analysis. *BioRxiv*: 060012.

993 Korsunsky, I., N. Millard, J. Fan, K. Slowikowski, F. Zhang, K. Wei, Y. Baglaenko, M.
994 Brenner, P.-r. Loh and S. Raychaudhuri. 2019. Fast, sensitive and accurate integration
995 of single-cell data with Harmony. *Nature methods* 16: 1289-1296.

996 Korsunsky, I., N. Millard, J. Fan, K. Slowikowski, F. Zhang, K. Wei, Y. Baglaenko, M.
997 Brenner, P. R. Loh and S. Raychaudhuri. 2019. Fast, sensitive and accurate integration
998 of single-cell data with Harmony. *Nat Methods* 16: 1289-1296.

999 Lee, J. S. and E. Rupp. 2019. Multiomics Prediction of Response Rates to Therapies
1000 to Inhibit Programmed Cell Death 1 and Programmed Cell Death 1 Ligand 1. *JAMA
1001 Oncol* 5: 1614-1618.

1002 Lee, M. G., R. Villa, P. Trojer, J. Norman, K. P. Yan, D. Reinberg, L. Di Croce and R.
1003 Shiekhattar. 2007. Demethylation of H3K27 regulates polycomb recruitment and H2A
1004 ubiquitination. *Science* 318: 447-450.

1005 Mazzarella, L., B. A. Duso, D. Trapani, C. Belli, P. D'Amico, E. Ferraro, G. Viale and G.
1006 Curigliano. 2019. The evolving landscape of 'next-generation' immune checkpoint
1007 inhibitors: A review. *Eur J Cancer* 117: 14-31.

1008 McBeath, R., D. M. Pirone, C. M. Nelson, K. Bhadriraju and C. S. Chen. 2004. Cell
1009 shape, cytoskeletal tension, and RhoA regulate stem cell lineage commitment. *Dev Cell*
1010 6: 483-495.

1011 McCrea, P. D. and J. I. Park. 2007. Developmental functions of the P120-catenin sub-
1012 family. *Biochim Biophys Acta* 1773: 17-33.

1013 Mimata, A., H. Fukamachi, Y. Eishi and Y. Yuasa. 2011. Loss of E-cadherin in mouse
1014 gastric epithelial cells induces signet ring-like cells, a possible precursor lesion of
1015 diffuse gastric cancer. *Cancer Sci* 102: 942-950.

1016 Muro, K., E. Van Cutsem, Y. Narita, G. Pentheroudakis, E. Baba, J. Li, M. H. Ryu, W. I.
1017 W. Zamaniah, W. P. Yong, K. H. Yeh, K. Kato, Z. Lu, B. C. Cho, I. M. Nor, M. Ng, L. T.
1018 Chen, T. E. Nakajima, K. Shitara, H. Kawakami, T. Tsushima, T. Yoshino, F. Lordick, E.
1019 Martinelli, E. C. Smyth, D. Arnold, H. Minami, J. Tabernero and J. Y. Douillard. 2019.
1020 Pan-Asian adapted ESMO Clinical Practice Guidelines for the management of patients
1021 with metastatic gastric cancer: a JSMO-ESMO initiative endorsed by CSCO, KSMO,
1022 MOS, SSO and TOS. *Ann Oncol* 30: 19-33.

1023 O'Connor, K. and M. Chen. 2013. Dynamic functions of RhoA in tumor cell migration
1024 and invasion. *Small GTPases* 4: 141-147.

1025 Oh, S. C., B. H. Sohn, J.-H. Cheong, S.-B. Kim, J. E. Lee, K. C. Park, S. H. Lee, J.-L.
1026 Park, Y.-Y. Park, H.-S. Lee, H.-J. Jang, E. S. Park, S.-C. Kim, J. Heo, I.-S. Chu, Y.-J.
1027 Jang, Y.-J. Mok, W. Jung, B.-H. Kim, A. Kim, J. Y. Cho, J. Y. Lim, Y. Hayashi, S. Song,
1028 E. Elimova, J. S. Estralla, J. H. Lee, M. S. Bhutani, Y. Lu, W. Liu, J. Lee, W. K. Kang, S.
1029 Kim, S. H. Noh, G. B. Mills, S.-Y. Kim, J. A. Ajani and J.-S. Lee. 2018. Clinical and
1030 genomic landscape of gastric cancer with a mesenchymal phenotype. *Nature
1031 Communications* 9: 1777.

1032 Oliveira, C., H. Pinheiro, J. Figueiredo, R. Seruca and F. Carneiro. 2015. Familial gastric
1033 cancer: genetic susceptibility, pathology, and implications for management. *Lancet
1034 Oncol* 16: e60-70.

1035 Ooki, A. and K. Yamaguchi. 2022. The dawn of precision medicine in diffuse-type
1036 gastric cancer. *Ther Adv Med Oncol* 14: 17588359221083049.

1037 Ran, F., P. D. Hsu, J. Wright, V. Agarwala, D. A. Scott and F. Zhang. 2013. Genome
1038 engineering using the CRISPR-Cas9 system. *Nature protocols* 8: 2281-2308.

1039 Riquelme, E., C. Behrens, H. Y. Lin, G. Simon, V. Papadimitrakopoulou, J. Izzo, C.
1040 Moran, N. Kalhor, J. J. Lee, J. D. Minna and Wistuba, II. 2016. Modulation of EZH2
1041 Expression by MEK-ERK or PI3K-AKT Signaling in Lung Cancer Is Dictated by Different
1042 KRAS Oncogene Mutations. *Cancer Res* 76: 675-685.

1043 Salt, M. B., S. Bandyopadhyay and F. McCormick. 2014. Epithelial-to-mesenchymal
1044 transition rewrites the molecular path to PI3K-dependent proliferation. *Cancer Discov* 4:
1045 186-199.

1046 Selim, J. H., S. Shaheen, W. C. Sheu and C. T. Hsueh. 2019. Targeted and novel
1047 therapy in advanced gastric cancer. *Exp Hematol Oncol* 8: 25.

1048 Stodden, G. R., M. E. Lindberg, M. L. King, M. Paquet, J. A. MacLean, J. L. Mann, F. J.
1049 DeMayo, J. P. Lydon and K. Hayashi. 2015. Loss of Cdh1 and Trp53 in the uterus
1050 induces chronic inflammation with modification of tumor microenvironment. *Oncogene*
1051 34: 2471-2482.

1052 Sun, D., X. Guan, A. E. Moran, L. Y. Wu, D. Z. Qian, P. Schedin, M. S. Dai, A. V.
1053 Danilov, J. J. Alumkal, A. C. Adey, P. T. Spellman and Z. Xia. 2022. Identifying
1054 phenotype-associated subpopulations by integrating bulk and single-cell sequencing
1055 data. *Nat Biotechnol* 40: 527-538.

1056 Sung, H., J. Ferlay, R. L. Siegel, M. Laversanne, I. Soerjomataram, A. Jemal and F.
1057 Bray. 2021. Global Cancer Statistics 2020: GLOBOCAN Estimates of Incidence and
1058 Mortality Worldwide for 36 Cancers in 185 Countries. *CA Cancer J Clin* 71: 209-249.

1059 Suo, S., Q. Zhu, A. Saadatpour, L. Fei, G. Guo and G. C. Yuan. 2018. Revealing the
1060 Critical Regulators of Cell Identity in the Mouse Cell Atlas. *Cell Rep* 25: 1436-1445
1061 e1433.

1062 Tan, S. H., Y. Swathi, S. Tan, J. Goh, R. Seishima, K. Murakami, M. Oshima, T. Tsuji, P.
1063 Phuah, L. T. Tan, E. Wong, A. Fatehullah, T. Sheng, S. W. T. Ho, H. I. Grabsch, S.
1064 Srivastava, M. Teh, S. Denil, S. Mustafah, P. Tan, A. Shabbir, J. So, K. G. Yeoh and N.
1065 Barker. 2020. AQP5 enriches for stem cells and cancer origins in the distal stomach.
1066 *Nature* 578: 437-443.

1067 Teng, M. W., S. F. Ngiow, A. Ribas and M. J. Smyth. 2015. Classifying Cancers Based
1068 on T-cell Infiltration and PD-L1. *Cancer Res* 75: 2139-2145.

1069 Till, J. E., C. Yoon, B. J. Kim, K. Roby, P. Addai, E. Jonokuchi, L. H. Tang, S. S. Yoon
1070 and S. Ryeom. 2017. Oncogenic KRAS and p53 Loss Drive Gastric Tumorigenesis in
1071 Mice That Can Be Attenuated by E-Cadherin Expression. *Cancer Res* 77: 5349-5359.

1072 Tong, M., C. Yu, J. Shi, W. Huang, S. Ge, M. Liu, L. Song, D. Zhan, X. Xia, W. Liu, J.
1073 Feng, W. Shi, J. Ji, J. Gao, T. Shi, W. Zhu, C. Ding, Y. Wang, F. He, L. Shen, T. Li and
1074 J. Qin. 2019. Phosphoproteomics Enables Molecular Subtyping and Nomination of
1075 Kinase Candidates for Individual Patients of Diffuse-Type Gastric Cancer. *iScience* 22:
1076 44-57.

1077 Van de Sande, B., C. Flerin, K. Davie, M. De Waegeneer, G. Hulselmans, S. Aibar, R.
1078 Seurinck, W. Saelens, R. Cannoodt, Q. Rouchon, T. Verbeiren, D. De Maeyer, J.
1079 Reumers, Y. Saeys and S. Aerts. 2020. A scalable SCENIC workflow for single-cell
1080 gene regulatory network analysis. *Nat Protoc* 15: 2247-2276.

1081 van Roy, F. and G. Berx. 2008. The cell-cell adhesion molecule E-cadherin. *Cell Mol
1082 Life Sci* 65: 3756-3788.

1083 Verma, S. K., X. Tian, L. V. LaFrance, C. Duquenne, D. P. Suarez, K. A. Newlander, S.
1084 P. Romeril, J. L. Burgess, S. W. Grant, J. A. Brackley, A. P. Graves, D. A. Scherzer, A.
1085 Shu, C. Thompson, H. M. Ott, G. S. Aller, C. A. Machutta, E. Diaz, Y. Jiang, N. W.
1086 Johnson, S. D. Knight, R. G. Kruger, M. T. McCabe, D. Dhanak, P. J. Tummino, C. L.
1087 Creasy and W. H. Miller. 2012. Identification of Potent, Selective, Cell-Active Inhibitors
1088 of the Histone Lysine Methyltransferase EZH2. *ACS Med Chem Lett* 3: 1091-1096.

1089 Wainberg, Z. A., C. S. Fuchs, J. Tabernero, K. Shitara, K. Muro, E. Van Cutsem, Y. J.
1090 Bang, H. C. Chung, K. Yamaguchi, E. Varga, J. S. Chen, D. Hochhauser, P. Thuss-
1091 Patience, S. E. Al-Batran, M. Garrido, U. Kher, C. S. Shih, S. Shah, P. Bhagia and J.
1092 Chao. 2021. Efficacy of Pembrolizumab Monotherapy for Advanced
1093 Gastric/Gastroesophageal Junction Cancer with Programmed Death Ligand 1
1094 Combined Positive Score >/=10. *Clin Cancer Res* 27: 1923-1931.

1095 Wang, R., M. Dang, K. Harada, G. Han, F. Wang, M. Pool Pizzi, M. Zhao, G.
1096 Tatlonghari, S. Zhang, D. Hao, Y. Lu, S. Zhao, B. D. Badgwell, M. Blum Murphy, N.
1097 Shanbhag, J. S. Estrella, S. Roy-Chowdhuri, A. A. F. Abdelhakeem, Y. Wang, G. Peng,
1098 S. Hanash, G. A. Calin, X. Song, Y. Chu, J. Zhang, M. Li, K. Chen, A. J. Lazar, A.
1099 Futreal, S. Song, J. A. Ajani and L. Wang. 2021. Single-cell dissection of intratumoral
1100 heterogeneity and lineage diversity in metastatic gastric adenocarcinoma. *Nat Med* 27:
1101 141-151.

1102 Wang, R., S. Song, K. Harada, F. Ghazanfari Amlashi, B. Badgwell, M. P. Pizzi, Y. Xu,
1103 W. Zhao, X. Dong, J. Jin, Y. Wang, A. Scott, L. Ma, L. Huo, D. Vicente, M. Blum
1104 Murphy, N. Shanbhag, G. Tatlonghari, I. Thomas, J. Rogers, M. Kobayashi, J.
1105 Vykoukal, J. S. Estrella, S. Roy-Chowdhuri, G. Han, S. Zhang, X. Mao, X. Song, J.
1106 Zhang, J. Gu, R. L. Johnson, G. A. Calin, G. Peng, J. S. Lee, S. M. Hanash, A. Futreal,
1107 Z. Wang, L. Wang and J. A. Ajani. 2020. Multiplex profiling of peritoneal metastases
1108 from gastric adenocarcinoma identified novel targets and molecular subtypes that
1109 predict treatment response. *Gut* 69: 18-31.

1110 Wang, S. C., Y. Yeu, S. T. G. Hammer, S. Xiao, M. Zhu, C. Hong, J. R. Clemenceau, L.
1111 Y. Yoon, I. Nassour, J. Shen, D. Agarwal, S. I. Reznik, J. C. Mansour, A. C. Yopp, H.
1112 Zhu, T. H. Hwang and M. R. Porembka. 2020. Hispanic/Latino Patients with Gastric
1113 Adenocarcinoma Have Distinct Molecular Profiles Including a High Rate of Germline
1114 CDH1 Variants. *Cancer Res* 80: 2114-2124.

1115 Weber, E. W., K. R. Parker, E. Sotillo, R. C. Lynn, H. Anbunathan, J. Lattin, Z. Good, J.
1116 A. Belk, B. Daniel, D. Klysz, M. Malipatlolla, P. Xu, M. Bashti, S. Heitzeneder, L.
1117 Labanieh, P. Vandris, R. G. Majzner, Y. Qi, K. Sandor, L. C. Chen, S. Prabhu, A. J.
1118 Gentles, T. J. Wandless, A. T. Satpathy, H. Y. Chang and C. L. Mackall. 2021. Transient
1119 rest restores functionality in exhausted CAR-T cells through epigenetic remodeling.
1120 *Science* 372.

1121 Wherry, E. J. and M. Kurachi. 2015. Molecular and cellular insights into T cell
1122 exhaustion. *Nat Rev Immunol* 15: 486-499.

1123 Wolf, F. A., P. Angerer and F. J. Theis. 2018. SCANPY: large-scale single-cell gene
1124 expression data analysis. *Genome Biol* 19: 15.

1125 Wolf, F. A., P. Angerer and F. J. Theis. 2018. SCANPY: large-scale single-cell gene
1126 expression data analysis. *Genome Biology* 19: 15.

1127 Wolock, S. L., R. Lopez and A. M. Klein. 2019. Scrublet: Computational Identification of
1128 Cell Doublets in Single-Cell Transcriptomic Data. *Cell Syst* 8: 281-291 e289.

1129 Young, M. D. and S. Behjati. 2020. SoupX removes ambient RNA contamination from
1130 droplet-based single-cell RNA sequencing data. *Gigascience* 9.

1131 Yu, W., N. Liu, X. Song, L. Chen, M. Wang, G. Xiao, T. Li, Z. Wang and Y. Zhang. 2023.
1132 EZH2: An Accomplice of Gastric Cancer. *Cancers (Basel)* 15.

1133

1134 **Figure Legends**

1135

1136 **Figure 1. CDH1 inactivation in DGAC patient tumor cells**

1137 **A.** Genetic alteration of the *CDH1* based on the cBioPortal stomach cancer datasets
1138 (<http://www.cbioportal.org>). n represents the total patients number enrolled in
1139 each subtype. DGAC, diffuse-type gastric adenocarcinoma; SRCC, signet ring
1140 cell carcinoma; TAC, tubular adenocarcinoma; STAD, stomach adenocarcinoma;
1141 MAC, mucinous adenocarcinoma; PAC, papillary adenocarcinoma.

1142 **B, C.** IHC staining of CDH1 in 114 DGAC patient tumor samples. The representative
1143 images are shown (B). Quantification of H score of CDH1 expression (C). *P*
1144 values were calculated using the one-way ANOVA; error bars: standard deviation
1145 (SD). Clinical information of 114 DGAC patients was showed in Table S4.

1146 **D.** Merged batch-based integrated UMAPs of 19 DGAC patients; integration
1147 package: Harmony. Clinical information of 19 DGAC patients was showed in
1148 Table S5.

1149 **E.** Merged Leiden-based integrated UMAP of 19 DGAC patients. Dashed line circle:
1150 epithelial cells. Epi: epithelial cells; Myeloid: myeloid cells; Effector T: effector T
1151 cells; Naïve T: naïve T cells; Exhausted T: exhausted T cells.

1152 **F.** Merged cell type-based UMAP of 19 DGAC patients. All cells were re-clustered
1153 according to the Leiden clusters and gathered as mega clusters. Dashed line
1154 circle: epithelial cells.

1155 **G.** Epithelial cells were re-clustered by Leiden.

1156 **H.** Correlation matrix plot of epithelial cells showing pair-wise correlations among all
1157 samples above. The dendrogram shows the distance of each dataset based on
1158 principal component analysis, and the Pearson correlation is displayed with a
1159 color spectrum. Groups of patients were categorized by dendrogram and
1160 correlation.

1161 **I.** Type-based heatmap of epithelial cells of merged datasets in 19 DGAC patients.
1162 Top 100 highly variable genes of each type were showed in Table S8.

1163 **J.** Type-based integrated and separated UMAPs of DGAC1 and DGAC2.

1164 **K.** Feature plots of epithelial cells displaying *CDH1* expression.

1165 **L.** Dot plots of epithelial cells of *CDH1* expression in different DGAC groups and
1166 individual patients.

1167 **M.** Molecular signatures of DGAC1 and DGAC2 patients. Top 50 highly variable
1168 genes were used to calculate the molecular signature of each group. Gene list
1169 was showed in Table S8. Dot plots of epithelial cells of each molecular signature
1170 in different subtypes and individual patient.

1172 **Figure 2. Comparative analyses of immune landscapes of DGAC subtypes**

1173 **A-B.** Cell type-based and Leiden-based UMAPs of DGAC1 and DGAC2.

1174 **C.** Absolute and relative cell proportions of individual patients and DGAC subtypes.

1175 Patients list was ranked by the DGAC group that they belong.

1176 **D.** Total cell-cell interactions from DGAC1 and DGAC2 were analyzed by using the

1177 CellChat package. More interactions were found in DGAC1.

1178 **E, F.** Differential number of interactions between DGAC1 and DGAC2 using circle

1179 plots (E) and heatmap (F). Red (or blue) colored edges (E) and squares (F)

1180 represent increased (or decreased) signaling in the DGAC1 compared to

1181 DGAC2.

1182 **G-I.** Score-based dot plot (G), feature plots (H), and dot plot of individual marker

1183 gene (I) of exhausted T cell score (markers are included in that score: *LAG3*,

1184 *TIGIT*, *CTLA4*, and *HAVCR2*). Genes that included in score analysis were

1185 showed in Table S9. *P* values were calculated by using a *t*-test.

1186 **J-L.** Score-based dot plot (J), feature plots (K), and dot plot of individual marker

1187 gene (L) of immune checkpoint score (markers are included in that score:

1188 *CTLA4*, *PDCD1*, *PDCD1LG2*, and *CD274*). Genes that included in score analysis

1189 were showed in Table S9. *P* values were calculated by using a *t*-test.

1190 **M-O.** Score-based dot plot (M), feature plots (N), and dot plot of individual marker

1191 gene (O) of exhausted T cell score (markers are included in that score: *IFITM1*,

1192 *JUNB*, *CLEC4E*, *IL1B*, *PLA2G7*, *ARG2*, *CLEC4D*, *CTSD*, and *CD84*). Genes that

1193 included in score analysis were showed in Table S9. *P* values were calculated by

1194 using a *t*-test.

1195

1196 **Figure 3. Establishment of genetically engineered gastric organoids with CDH1-**

1197 **inactivation**

1198 **A.** Genetic alteration of the *KRAS*, and *TP53* genes based on the cBioPortal. n

1199 represents the total patients number enrolled in each subtype. DGAC, diffuse-

1200 type gastric adenocarcinoma; SRCC, signet ring cell carcinoma; TAC, tubular

1201 adenocarcinoma; STAD, stomach adenocarcinoma; MAC, mucinous

1202 adenocarcinoma; PAC, papillary adenocarcinoma.

1203 **B.** Illustration of the workflow for stomach tissue collection and dissociation, gene

1204 manipulation of the gastric organoids (GOs), GOs culture, and representative

1205 image of GOs. Three GO lines were generated, including WT, KP, and EKP. WT

1206 mice and KP mice were sacrificed to collect stomach tissue. After removing

1207 forestomach, stomach tissue was dissociated into single cell and culture as

1208 organoids. Adeno-Cre virus was used to treat *Kras*^{LSL-G12D}; *Trp53*^{fl/fl} organoids to

1209 generate KP organoids, followed by nutlin-3 selection. After selection, EKP

1210 organoids were generated using CRISPR-mediated *Cdh1* KO from KP GOs.

1211 **C.** Representative images of WT, KP, and EKP GOs at passage day 8. Scale bar:
1212 200 μ m.

1213 **D.** Growth analysis for WT, KP, and EKP GOs in two passages at day 8 of each
1214 passage. P values were calculated using the one-way ANOVA; error bars: SD.
1215 Numbers below each label represent the number of organoids.

1216 **E.** Hematoxylin and eosin (H & E) staining of WT, KP, and EKP GOs.

1217 **F.** MKI67 staining of WT, KP, and EKP GOs (n=5).

1218 **G.** CDH1 staining of WT, KP, and EKP GOs (n=5).

1219 **H.** Statistics analysis of MKI67 staining (Figure 3F). P values were calculated using
1220 the one-way ANOVA; error bars: SD. The representative images are shown.

1221 **I.** Batch-based UMAPs of WT, KP, and EKP GOs. The Harmony integration package
1222 was used to remove the batch effect.

1223 **J.** Leiden-based clustering UMAPs of WT, KP, and EKP GOs. Cell clusters were
1224 named by the most highly variable genes.

1225 **K.** Cell proportion analysis of WT, KP, and EKP GOs. Each color represents a
1226 different cell type. The color code is based on the cell types shown in Figure 3J.

1227 **L.** Batch-based and Scissor-based UMAP of WT and EKP GOs generated by
1228 Scissor package. TCGA datasets of normal stomach and DGAC patients were
1229 utilized.

1230 **M.** Cluster-based and Scissor-based UMAP of EKP GOs generated by Scissor
1231 package. DGAC1 and DGAC2 datasets were utilized to perform the comparison.

1232 **N.** Dot plots of EKP GOs of DGAC1 and DGAC2 molecular signatures. Top 50
1233 highly variable genes were used to calculate the molecular signature of each
1234 DGAC subtype. Gene list was showed in Table S8.

1235

1236 **Figure 4. CDH1 KO promotes KP-driven gastric tumorigenesis**

1237 **A.** Bright-field images of KP and EKP cells in low and high magnification.

1238 **B.** Crystal violet staining of KP and EKP GOs-derived cells.

1239 **C.** Bright-field images of KP and EKP allograft tumors; tumor incidence of allograft
1240 tumors.

1241 **D, E.** Plot for tumor mass (D) and tumor size (E) assessment of KP and EKP
1242 allografts.

1243 **F.** H & E staining of KP and EKP allograft tumors (n \geq 3).

1244 **G, H.** MKI67 (G) and E-Cadherin (H) staining of KP and EKP allograft tumors (n \geq 3).
1245 Left images: low magnification. Right images: high magnification. Scale bars
1246 were shown on the representative images.

1247 **I.** Statistics analysis of MKi67 staining in Figure 4G. *P* values were calculated using
1248 Student's *t*-test; error bars: SD.

1249 **J-O.** CD3 (J), CD4 (K), CD8 (L), PDCD1 (M), TIM3 (N) staining and CD11B/LY6G
1250 co-staining (O) of KP and EKP allograft tumors (n≥3). Middle and Cortex
1251 represents the middle and cortex of the tumor, respectively. In each panel, left
1252 images showed low magnification, and right images showed high magnification.
1253 Scale bars were shown on the representative images.

1254 **P-U.** Statistics analysis of CD3 (P), CD4 (Q), CD8 (R), PDCD1 (S), TIM3 (T)
1255 staining and CD11B/LY6G co-staining (U). The positive cell percentage indicates
1256 the area of cells expressing a specific marker divided by the total field occupied
1257 cells stained by DAPI in the same area, which allows for normalization. Md:
1258 Middle; Ct: Cortex. *P* values were calculated using the one-way ANOVA; error
1259 bars: SD.

1260

1261 **Figure 5. *CDH1* KO-activated EZH2 promotes gastric tumorigenesis**

1262 **A.** Integrated batch-based and regulon pattern-based UMAP for WT, KP, and EKP
1263 GOs. Six transcriptional modules were identified.

1264 **B.** Separated regulon patterns based UMAP for WT, KP, and EKP GOs.

1265 **C.** Flow chart of regulons selection process.

1266 **D.** Regulons enriched in WT, KP, and EKP GOs, based on Z Score. 32 regulons
1267 were highly expressed in EKP samples compared to WT and KP.

1268 **E.** Regulons enriched in WT, KP, and EKP GOs, based on Regulon Specificity
1269 Score (RSS). The top 20 were selected by Z score. The whole regulon list based
1270 on RSS was showed in Table S18.

1271 **F.** Venn diagram for the regulons from figure 5D and 5E. 20 regulons were
1272 overlapped.

1273 **G.** Dot plot of the regulons (WT, KP and EKP GOs) increased in TCGA DGAC
1274 patients.

1275 **H.** Regulon activity-based UMAP of Ezh2 in WT, KP, and EKP GOs. The cells with
1276 lighter color represent regulated by Ezh2.

1277 **I, J.** Dot plots of EZH2 downstream target genes (I, genes which are downregulated
1278 by EZH2 activation through histone modification; J, genes which are
1279 downregulated by EZH2 activation reported in gastric cancer) scores in the
1280 epithelial cells of DGAC1 and DGAC2. Gene list of EZH2 targeted genes was
1281 listed in Table S9.

1282 **K.** The level of H3K27Ac and H3K27Me3 expression in KP and EKP allografts.
1283 Quantification was displayed.

1284 **L.** Crystal violet staining of KP and EKP cells after GSK343 (EZH2 inhibitor, 10 μ M,
1285 96 hrs).

1286 **M.** Bright field images (M) of KP and EKP GOs after treating with GSK343 (EZH2
1287 inhibitor, 10 μ M, 96 hrs). D2: day2; D6: day6.

1288 **N.** Statistical analysis of KP and EKP gastric organoid size and number in response
1289 to GSK343 treatment. The number of organoids (right Y-axis) and their size (left
1290 Y-axis) were assessed following treatment with GSK343. At Day 2 (D2), the
1291 number of organoids was determined for the image depicted in figure 5M, and
1292 this count was considered as 100% (n numbers are presented in the bubble plot).
1293 At Day 6 (D6), the number of organoids in the same field for each group was
1294 counted (n numbers also displayed in the bubble plot). The percentage of each
1295 group on D6 was calculated by dividing the number of viable organoids at D6 by
1296 the number at D2. The viable percentage is presented in the bar graph.

1297 **O-Q.** Transplantation of EKP cells followed by EZH2 inhibition. Bright-field images of
1298 EKP allograft tumors treated with DMSO and GSK343 (20 mg/kg) separately (O).
1299 Tumor growth curve of EKP allografts treated with DMSO and GSK343 (20
1300 mg/kg) after cell subcutaneous transplantation (P). Tumor mass of EKP allografts
1301 treated with DMSO and GSK343 (20 mg/kg) after mice scarification (Q). *P* values
1302 were calculated using Student's *t*-test; error bars: SD.

1306 **Supplementary Figures**

1307

1308 **Supplementary Figure S1. Transcriptional, clinical, and molecular**
1309 **characterization of DGAC subtypes**

1310 **A.** Dot plots of epithelial cell, myeloid cell, B cell, plasma cell, T cell, effector T cell,
1311 naïve T cell, exhausted T cell, fibroblast, and endothelial cell markers in merged
1312 19 DGAC patients scRNA-seq data.

1313 **B.** Leiden-based heatmap of all cells of merged datasets with annotation in 19
1314 DGAC patients. The most highly variable 100 genes of each cluster were showed
1315 in Table S6.

1316 **C.** Leiden-based heatmap of epithelial cells of merged datasets in 19 DGAC
1317 patients. The most highly variable 100 genes of each cluster were showed in
1318 Table S7.

1319 **D-G.** Venn diagram illustrating 19 DGAC patient groups with survival, race,
1320 pathology, and gender data. Long-term survivors (surviving over 1-year post-
1321 diagnosis) and short-term survivors (deceased within 6 months post-diagnosis)
1322 were classified according to our previous publication (Wang et al., 2021).

1323 **H.** Metastatic sites of DGAC1 and DGAC2 patients.

1324 **I.** Age difference between DGAC1 and DGAC2 patients.

1325 **J-R.** Dot plots, violin plots, and feature plots of EMT (J), FGFR2 (K), FGFR1 (L),
1326 PI3K_AKT_MTOR (M), RHOA (N), MAPK (O), HIPPO (P), WNT (Q), and
1327 TGFbeta (R) scores in two DGAC types. *P* values were calculated by using a *t*-
1328 test. The genes included in each score are listed in Table S9.

1329

1330 **Supplementary Figure S2. scRNA-seq analysis of 19 DGAC patients and 29**
1331 **adjacent normal stomach tissue**

1332 **A.** Merged batch-based UMAP of 29 adjacent normal stomach tissue (Normal
1333 tissue) and 19 DGAC patients. Total cell numbers are 249080. Integration
1334 package: Harmony.

1335 **B.** Annotated Leiden-based integrated UMAPs of 19 DGAC patients and 29 adjacent
1336 normal stomach tissue. Epi: Epithelial cells; Myeloid: myeloid cells; Effector T:
1337 effector T cells; Naïve T: Naïve T cells; Exhausted T: Exhausted T cells;
1338 Endothelial: Endothelial cells.

1339 **C.** Dot plots of epithelial cell, myeloid cell, B cell, plasma cell, T cell, effector T cell,
1340 naïve T cell, exhausted T cell, fibroblast, and endothelial cell markers in merged
1341 19 DGAC patients and 29 adjacent normal stomach tissue scRNA-seq data.

1342 **D.** Merged Leiden-based integrated UMAPs of 29 adjacent normal stomach tissue
1343 (Normal tissue) and 19 DGAC patients. Epi: epithelial cells; Myeloid: myeloid

1344 cells; Effector T: effector T cells; Naïve T: naïve T cells; Exhausted T: exhausted
1345 T cells. The most highly variable 100 genes of each cluster were showed in
1346 Table S10.

1347 **E.** Merged cell type-based UMAP of 29 Normal tissue and 19 DGAC patients. All
1348 cells were re-clustered according to the Leiden clusters and gathered as mega
1349 clusters. Dashed line-circle: epithelial cells.

1350 **F.** Type-based heatmap of all cells of merged datasets in 19 DGAC patients and 29
1351 adjacent normal stomach tissue.

1352 **G.** Separated UMAPs of Normal tissue and two types of DGACs. Dashed line-circle:
1353 epithelial cells.

1354 **H.** CNV heatmap of DGAC1 and DGAC2, tumor-adjacent normal stomach tissue
1355 (Normal) was used as reference for the CNV inference. Red: copy number gain
1356 (CNG); blue: copy number loss (CNL)

1357 **I.** CNV heatmap of DGAC1 and DGAC2, tumor-adjacent normal stomach tissue
1358 (Normal) was used as reference for the CNV inference.

1359 **J.** Statistics analysis of CNV score of all cells (left panel) and epithelial cells (right
1360 panel) among Normal, DGAC1, and DGAC2. *P* values were calculated using the
1361 one-way ANOVA; error bars: SD.

1362 **K, L.** Individual cell type-based UMAP of the patients in DGAC1 and DGAC2.
1363 DGAC1 patients were enriched with stromal cells, mainly T cells. DGAC2
1364 patients were enriched with epithelial cells.

1365

1366 **Supplementary Figure S3. GSEA analysis and the expression of macrophage**
1367 **polarization markers of DGAC1 and DGAC2.**

1368 **A-F.** GSEA analysis comparing DGAC1 to DGAC2 using DGAC2 as the reference
1369 gene set. Enriched pathways in DGAC1 are displayed in the upper green panel,
1370 while those in DGAC2 are shown in the lower blue panel. Pathway datasets
1371 analyzed include GOBP (A), REACTOME (B), WP (C), BIOCARTA (D), PID (E),
1372 and KEGG (F). Pathways with positive NES (Normalized Enrichment Score)
1373 indicate enrichment in DGAC1, while those with negative NES indicate
1374 enrichment in DGAC2. GOBP: Gene ontology biological process; REACTOME:
1375 Reactome gene sets; WP: WikiPathways gene sets; BIOCARTA: BioCarta gene
1376 sets; PID: PID gene sets; KEGG: KEGG gene sets. Pathways related with
1377 immune response were enriched in DGAC1 based on GOBP, WP, BIOCARTA,
1378 PID, and KEGG.

1379 **G, H.** Dot plot of macrophage polymerization markers in DGAC1 and DGAC2. Most
1380 of the M1 and M2 markers are enriched in DGAC1, except for STAT1 and
1381 VEGFA.

1383 **Supplementary Figure S4. Validation of genetic engineering and scRNA-seq**
1384 **analysis of mouse GOs**

1385 **A-C.** Genotyping results of KP organoids (A and B). After adeno-Cre treatment, KP
1386 organoids lost *Trp53*, while *Kras*^{G12D} was activated in KP organoids. After *Cdh1*
1387 CRISPR knock out (KO), we performed sanger sequencing to compare the
1388 sequence of *Cdh1* in WT and EKP (C). The five targeting sequences against
1389 *Cdh1* were showed in methods ‘**CRISPR/Cas9-based gene knockout in GOs**’.
1390 The primers used for genotyping were showed in Table S2.

1391 **D.** Illustration of the workflow for stomach tissue collection and dissociation, gene
1392 manipulation of the gastric organoids (GOs), sample preparation of multiplex
1393 scRNA sequencing.

1394 **E.** Workflow of single cell library preparation.

1395 **F.** Heatmap of each cell clusters of merged datasets, including WT, KP, and EKP.

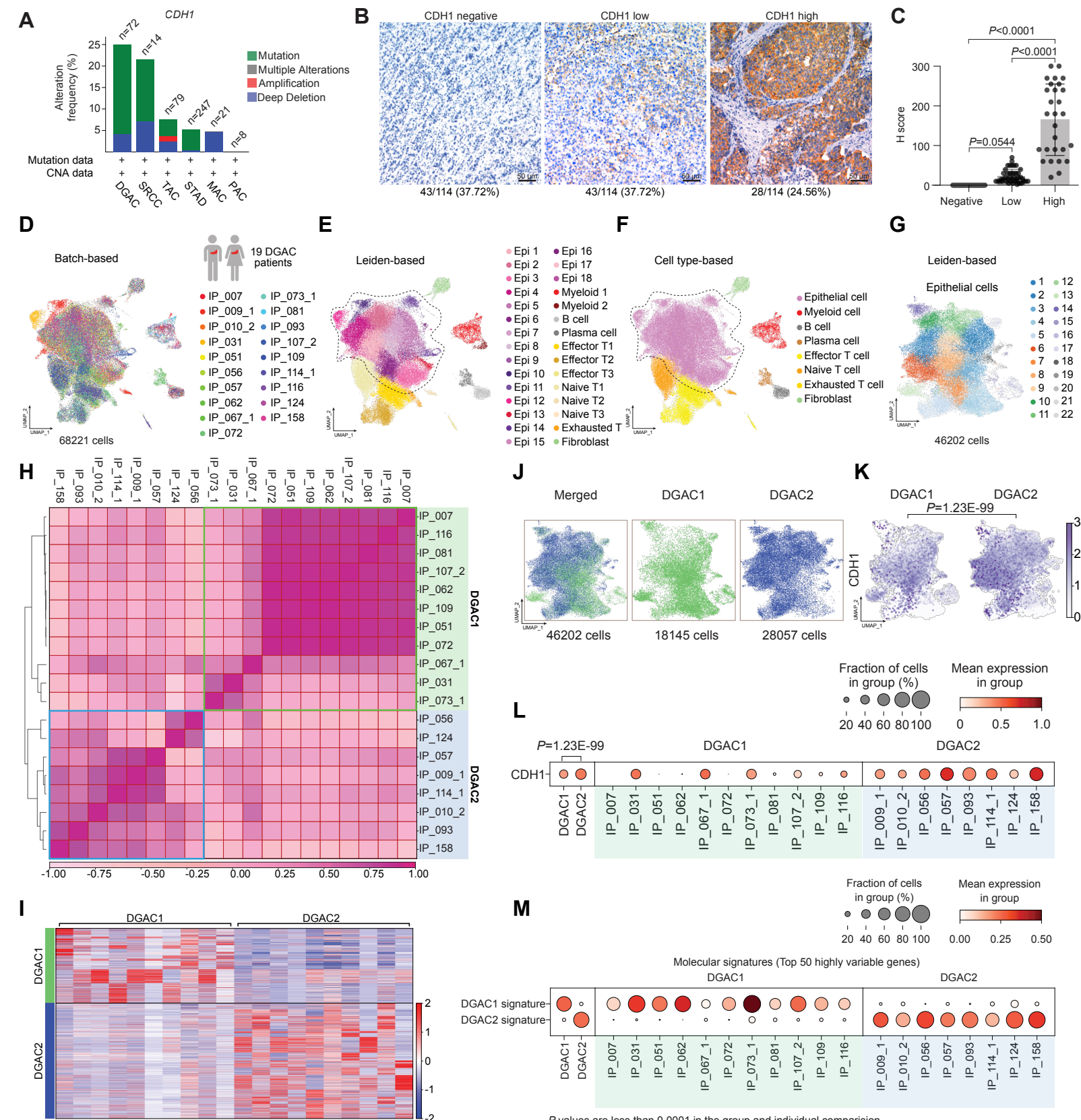
1396 **G-I.** Separate heatmap of each cell clusters of WT, KP, and EKP datasets,
1397 respectively.

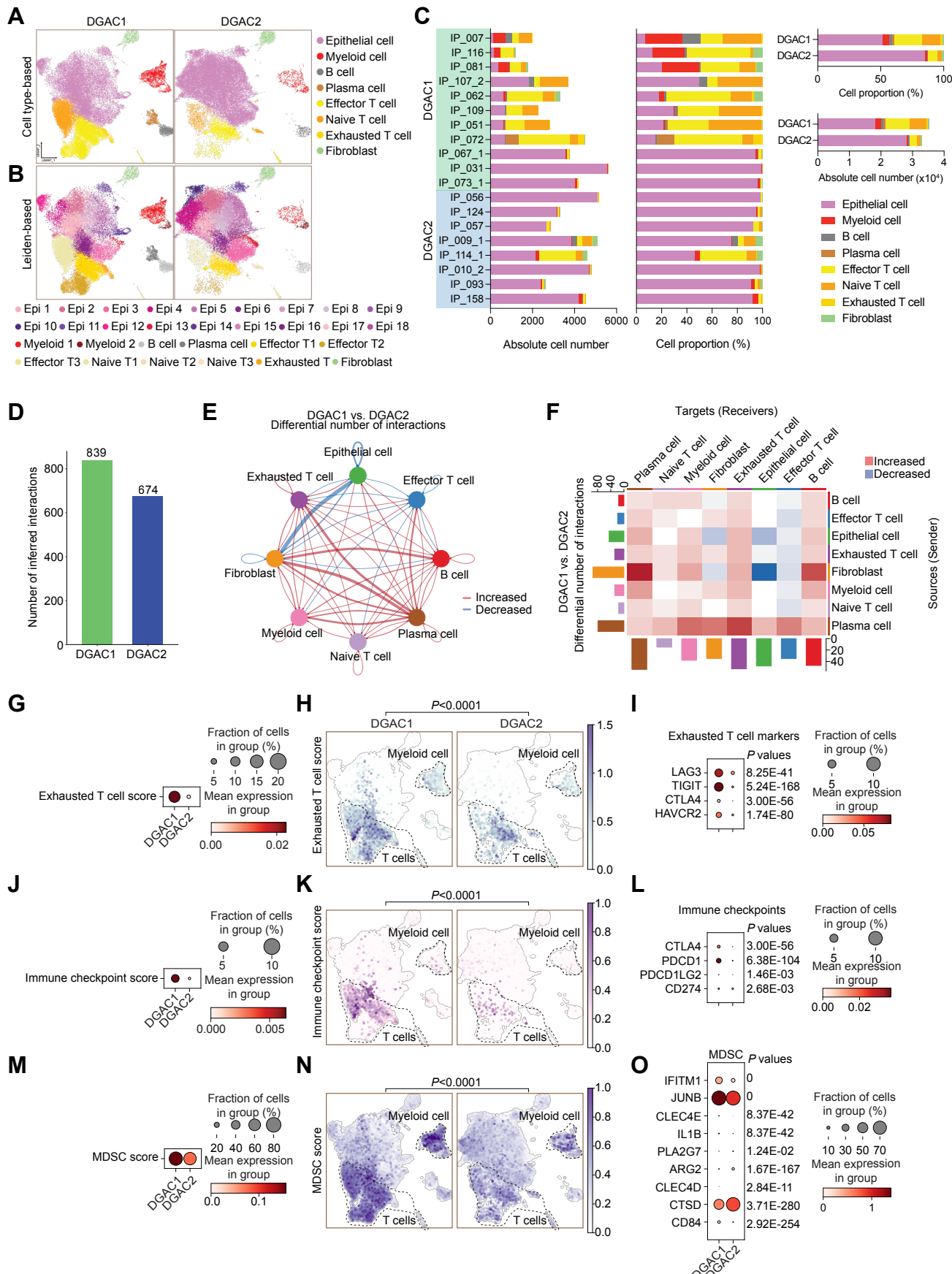
1399 **Supplementary Figure S5. EKP-specific regulons expression and EZH2**
1400 **downstream targeted genes expression**

1401 **A.** The expression of 20 regulons in TCGA DGAC patients and normal stomach.

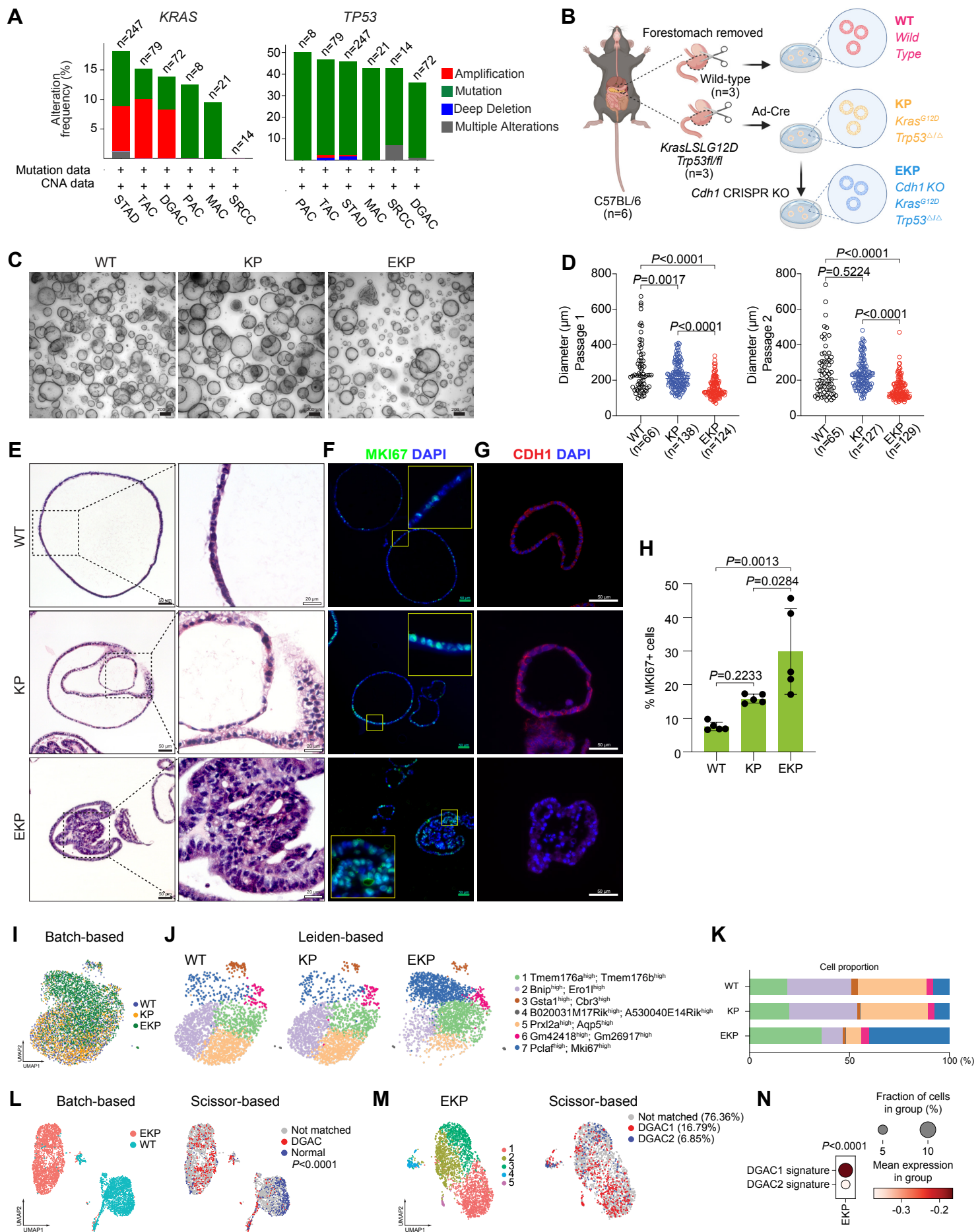
1402 **B.** Regulon activity based UMAP of *Gtf2b*, *Pole4*, and *Sox4*. *P* values were
1403 calculated by using the Student’s *t*-test; error bars: SD.

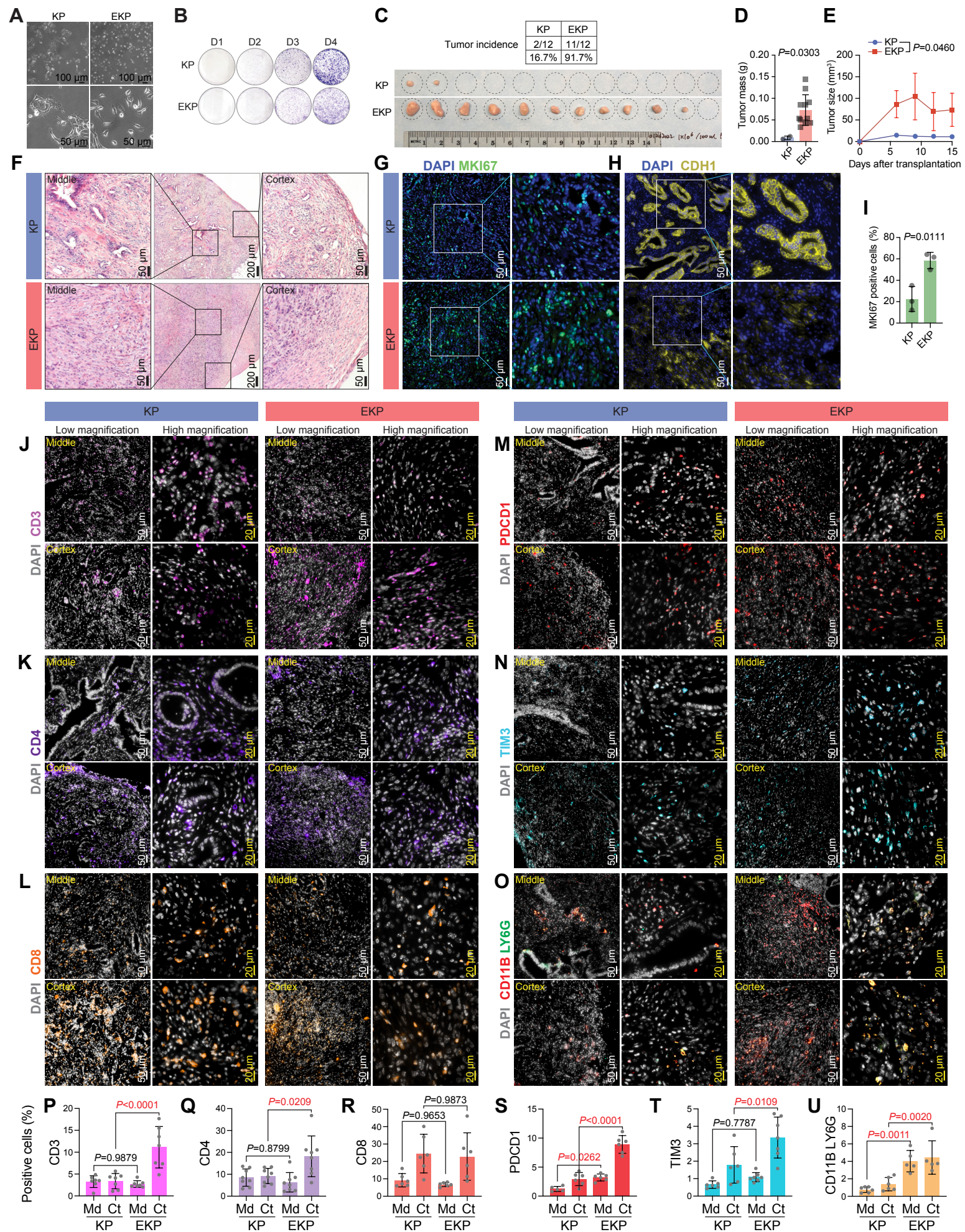
1404 **C, D.** Violin (left panel) and feature plots (right panel) of EZH2 downstream target
1405 genes (C, genes which are downregulated by EZH2 through histone modification;
1406 D, genes which are downregulated by EZH2 reported in gastric cancer) scores in
1407 the epithelial cells of DGAC1 and DGAC2. Gene list of EZH2 targeted genes was
1408 listed in Table S9.



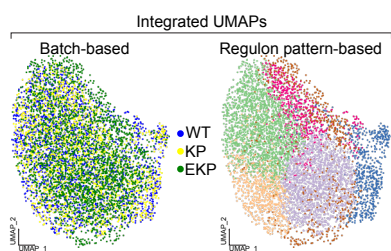


RFigure 3

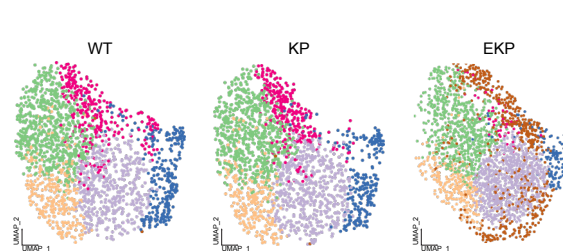




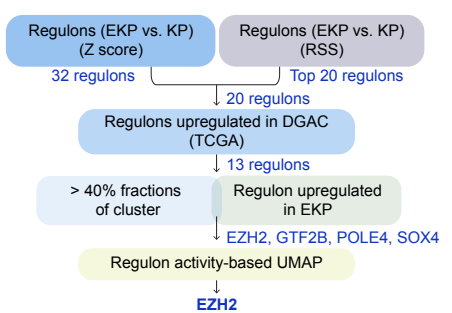
A



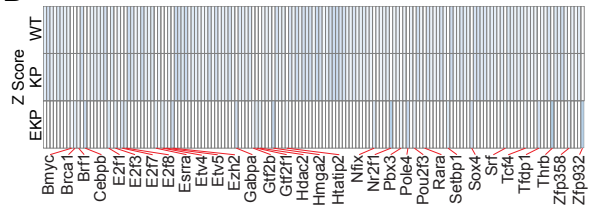
B



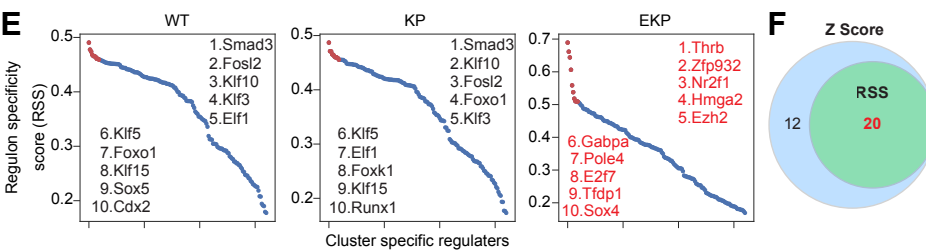
C



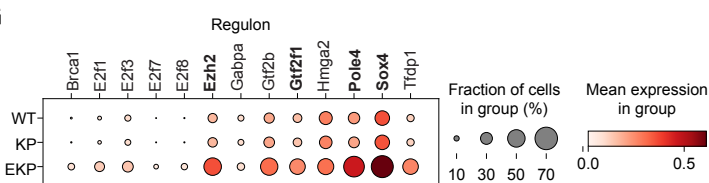
D



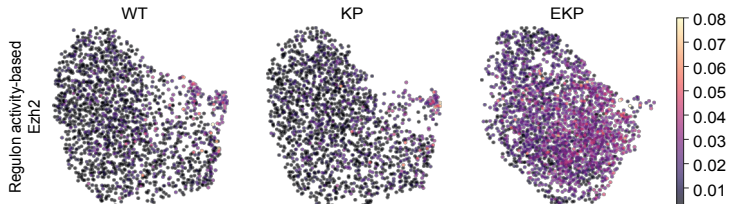
E



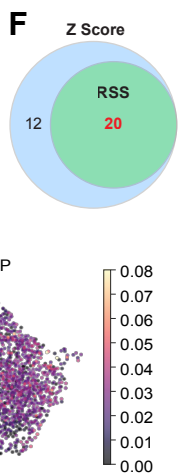
G



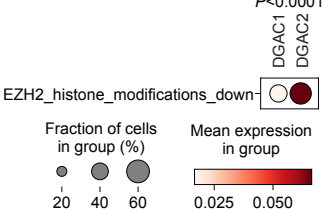
H



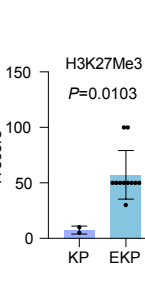
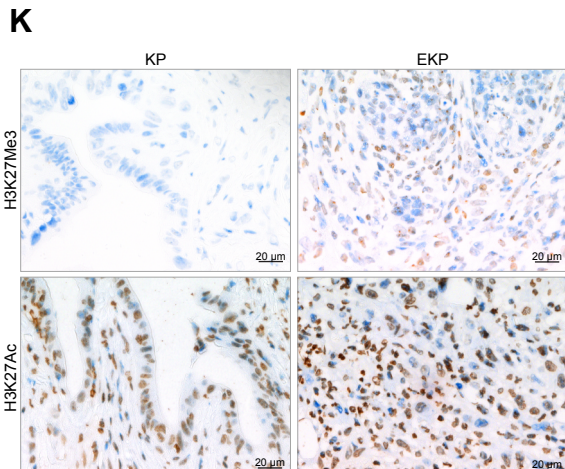
F



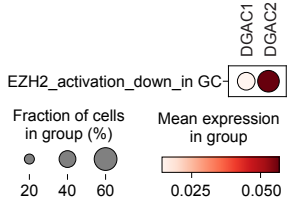
I



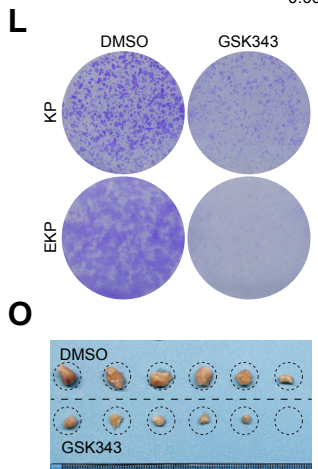
K



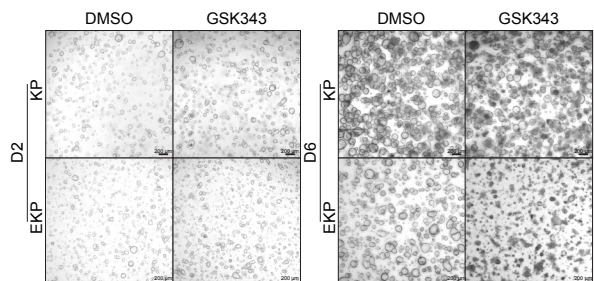
J



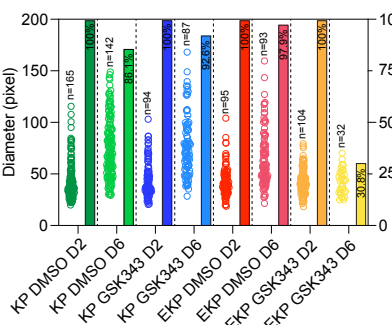
L



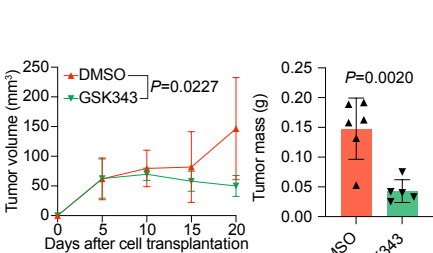
M



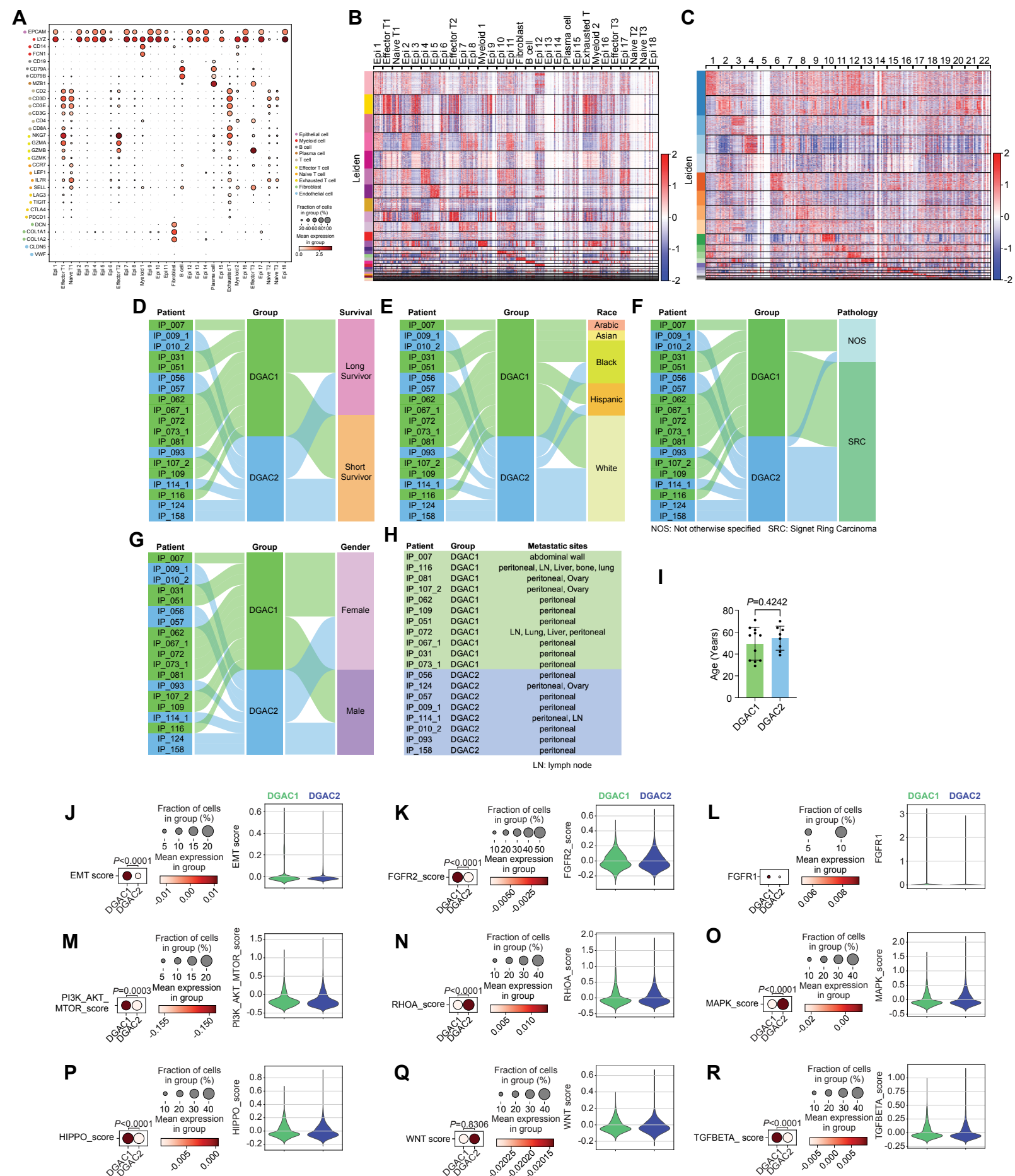
N



P

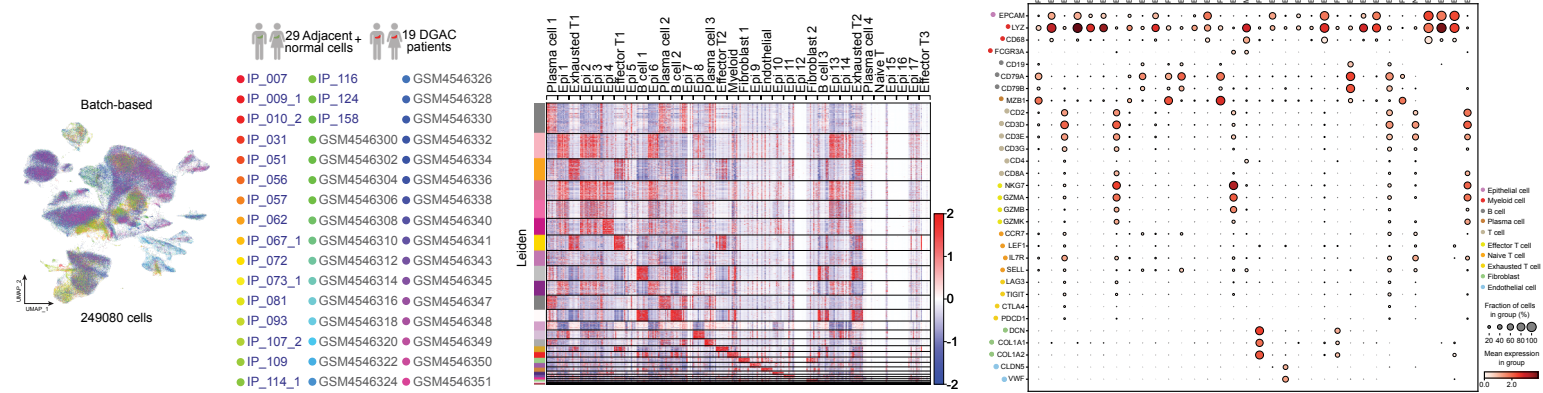


Q

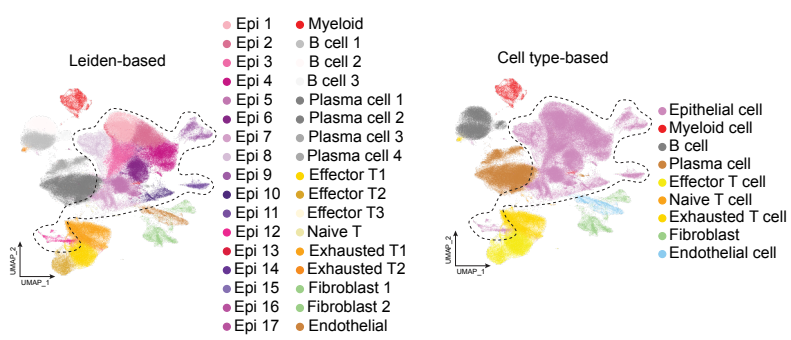


bioRxiv preprint doi: <https://doi.org/10.1101/2023.09.11.570000>; this version posted September 11, 2023. The copyright holder for this preprint (which was not certified by peer review) is the author/funder, who has granted bioRxiv a license to display the preprint in perpetuity. It is made available under a [aCC-BY-ND 4.0 International license](https://creativecommons.org/licenses/by-nd/4.0/).

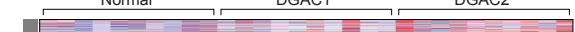
A



D

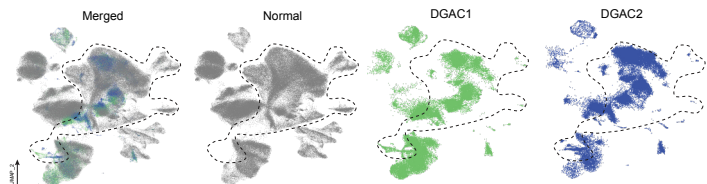


F

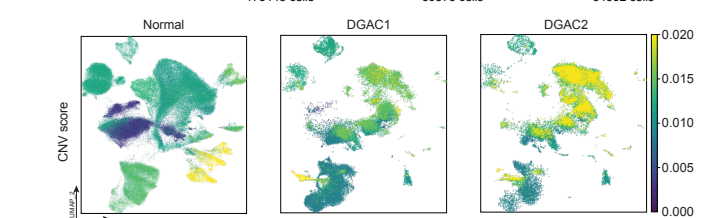


DGAC2

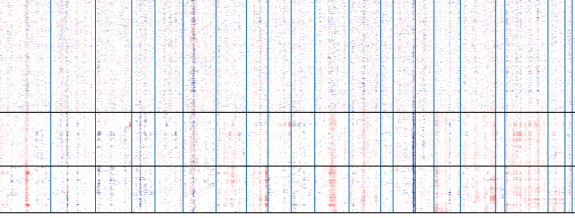
G



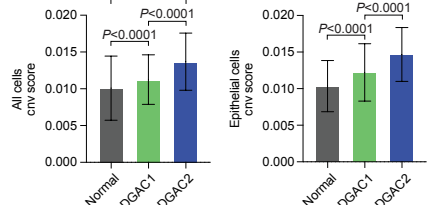
16 17 18



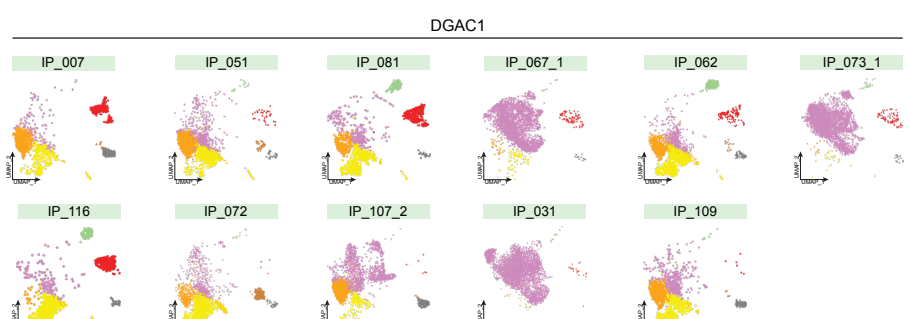
10



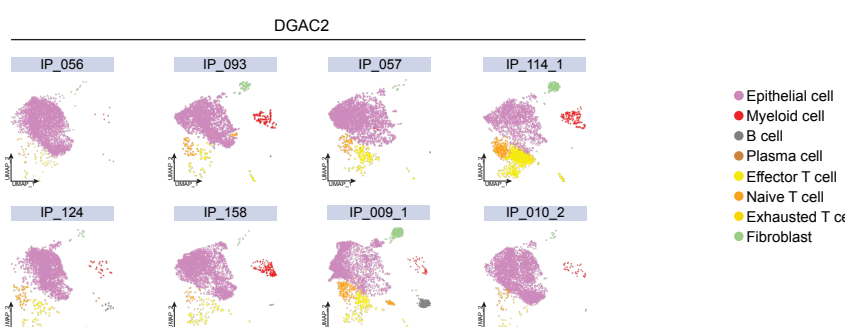
1



K

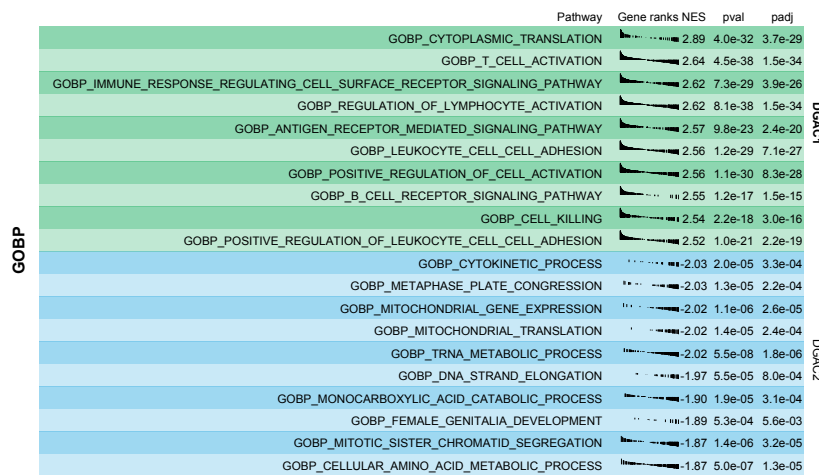


1

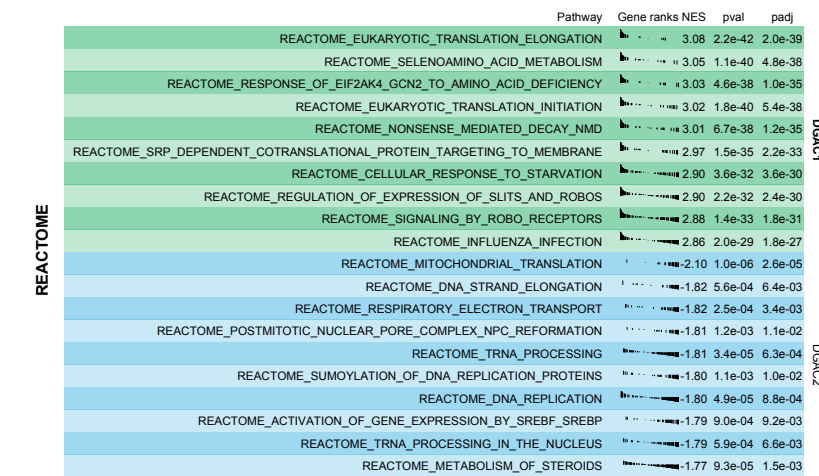


Supplementary Figure S3

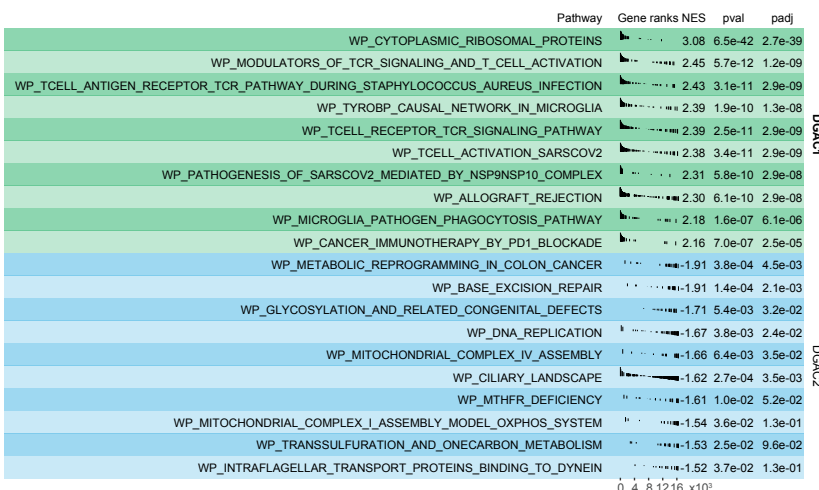
A



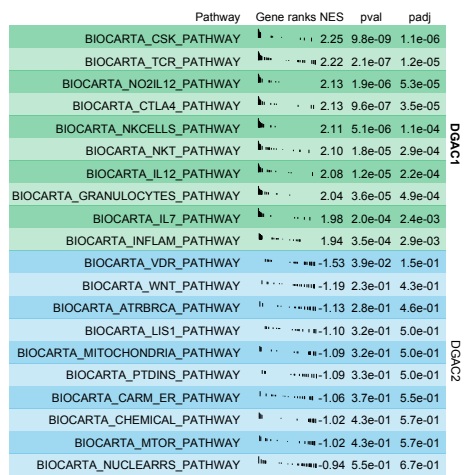
B



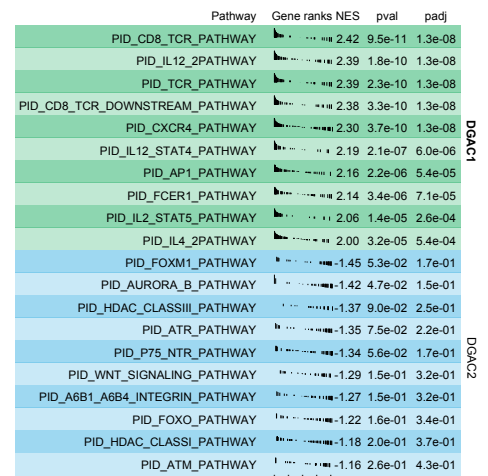
C



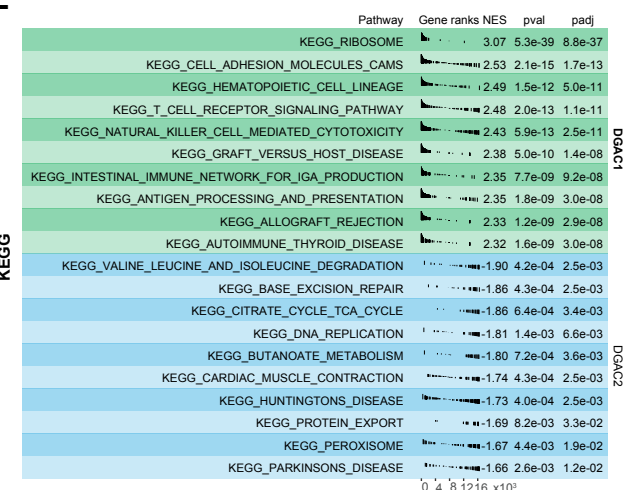
D



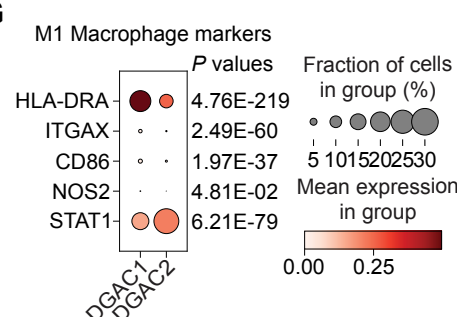
E



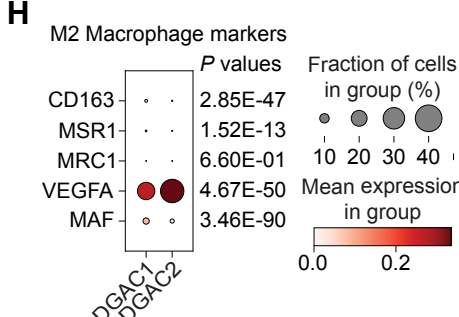
F



G

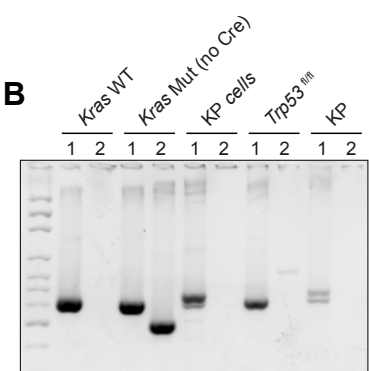
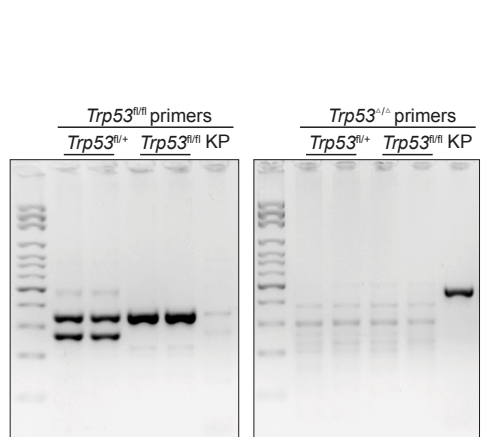


H



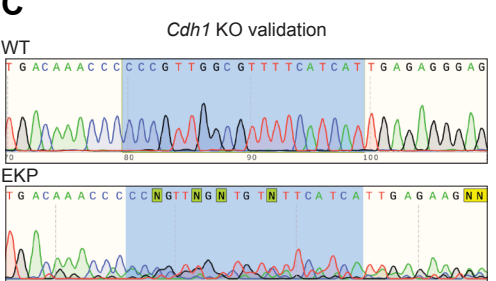
Supplementary Figure S4

A

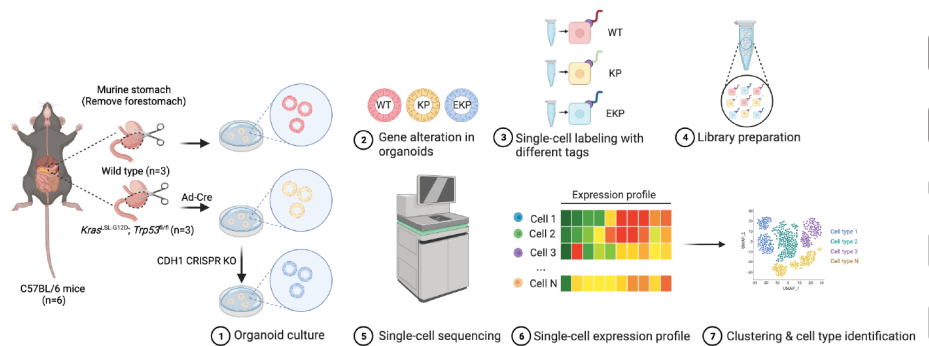


Primer set 1: Kras WT; Kras G12D Mutant (After Cre; Activated Kras)
Primer set 2: Kras G12D Mutant (Before Cre)

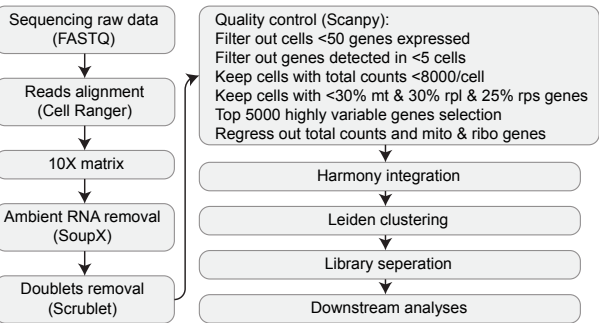
C



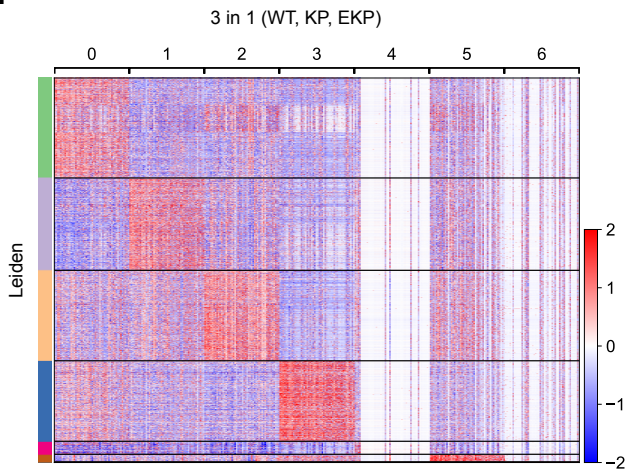
D



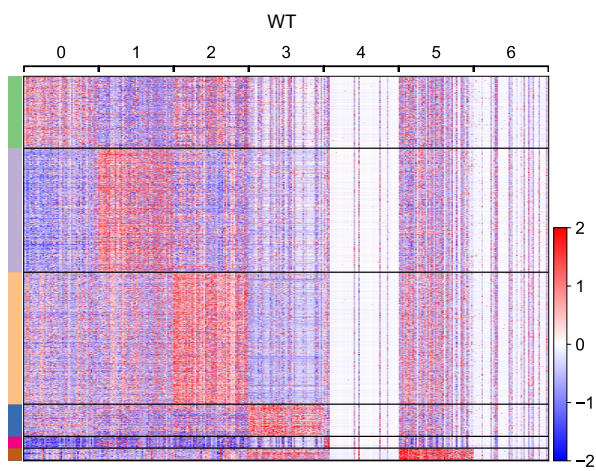
E



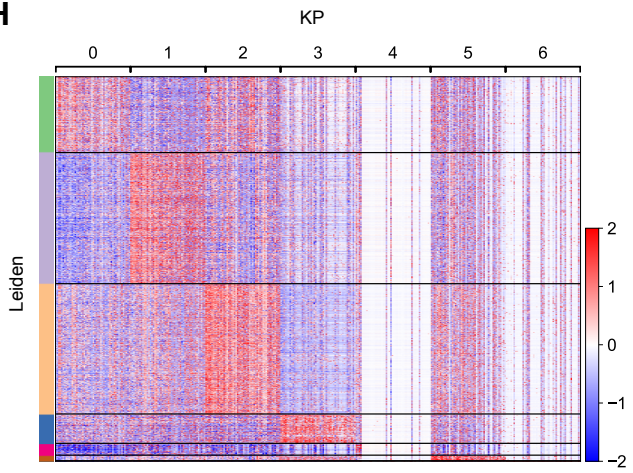
F



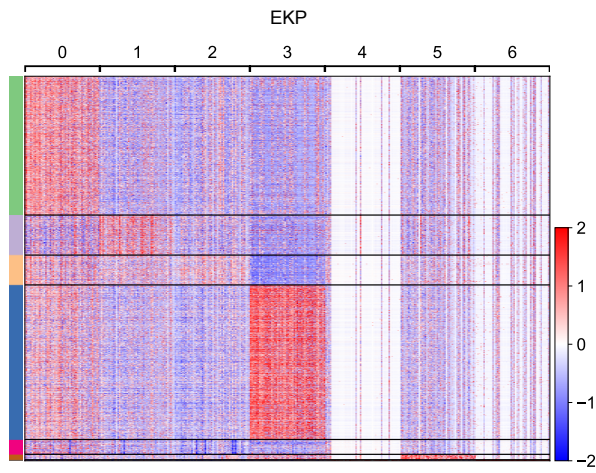
G



H



I



Legend for expression heatmap:

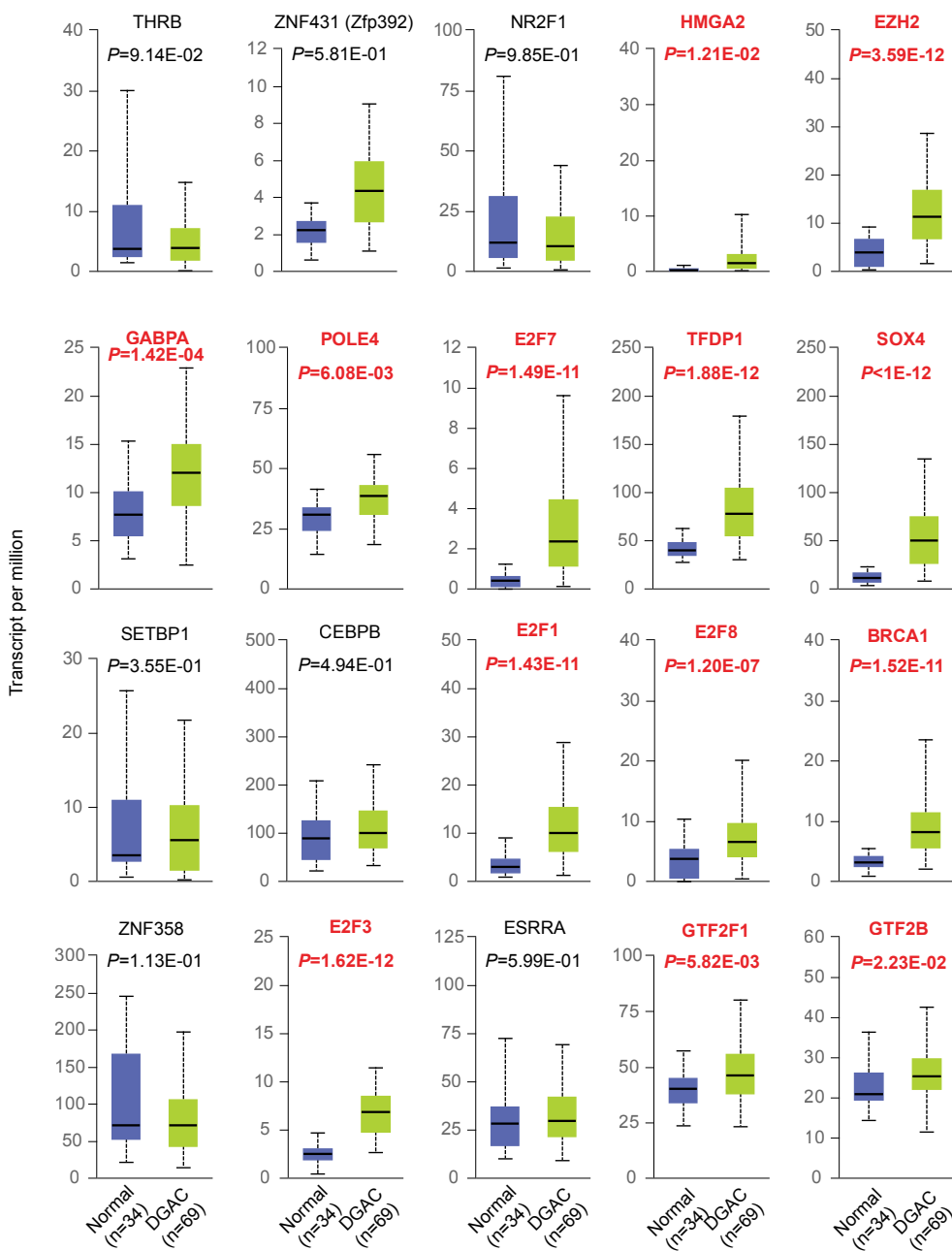
- 1 Tmem176a^{high}; Tmem176b^{high}
- 2 Bnip^{high}; Ero1^{high}
- 3 Gsta1^{high}; Cbr3^{high}
- 4 B020031M17Rik^{high}; A530040E14Rik^{high}
- 5 Prxl2a^{high}; Aqp5^{high}
- 6 Gm42418^{high}; Gm26917^{high}
- 7 Pclaf^{high}; Mki67^{high}

Supplementary Figure S5

A

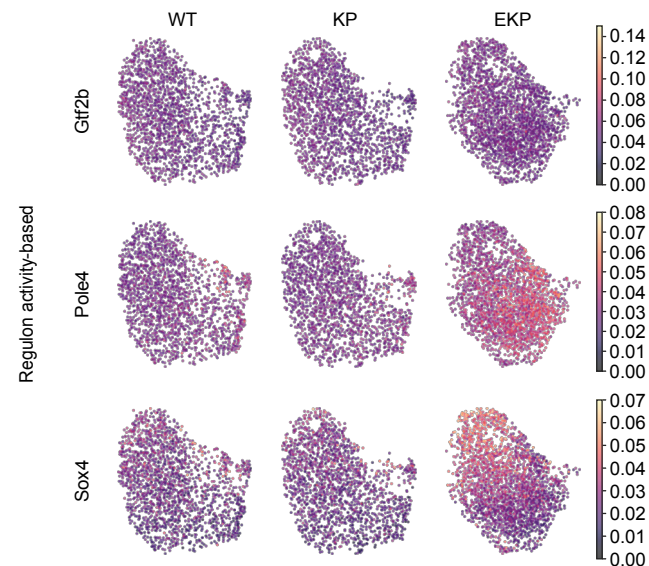
Bold: Statistically significance

Regular: No significance



B

TCGA STAD samples



C

EZH2_histone_modifications_down

